

Automatic Breast Ultrasound Image Segmentation: A Survey

Min Xian¹, Yingtao Zhang², H. D. Cheng¹, Fei Xu¹, Boyu Zhang¹, Jianrui Ding²

¹*Department of Computer Science, Utah State University, Logan, UT 84322, USA*

²*School of Computer Science and Technology, Harbin Institute of Technology, China*

Abstract

Breast cancer is one of the leading causes of cancer death among women worldwide. In clinical routine, automatic breast ultrasound (BUS) image segmentation is very challenging and essential for cancer diagnosis and treatment planning. Many BUS segmentation approaches have been studied in the last two decades, and have been proved to be effective on private datasets. Currently, the advancement of BUS image segmentation seems to meet its bottleneck. The improvement of the performance is increasingly challenging, and only few new approaches were published in the last several years. It is the time to look at the field by reviewing previous approaches comprehensively and to investigate the future directions. In this paper, we study the basic ideas, theories, pros and cons of the approaches, group them into categories, and extensively review each category in depth by discussing the principles, application issues, and advantages/disadvantages.

Keyword: breast ultrasound (BUS) images, breast cancer, segmentation, benchmark, early detection, computer-aided diagnosis (CAD)

1. Introduction

Breast cancer occurs in the highest frequency in women among all cancers, and is also one of the leading causes of cancer death worldwide [1, 2]. Scientists do not definitely know what causes breast cancer, and only know some risk factors that can increase the likelihood of developing breast cancer: getting older, genetics, radiation exposure, dense breast tissue, alcohol consumption, etc. The key of reducing the mortality is to find signs and symptoms of breast cancer at its early stage by clinic examination [3]. Breast ultrasound (BUS) imaging has become one of the most important and effective modality for the early detection of breast cancer because of its noninvasive, nonradiative and cost-effective nature [4]; and it is most suitable for large scale breast cancer screening and diagnosis in low-resource countries and regions.

Computer-Aided Diagnosis (CAD) systems based on B-mode breast ultrasound have been developed to overcome the considerable inter- and intra-variabilities of the breast cancer diagnosis, and have been clinically-tested their ability to improve the performance of the breast cancer diagnosis. BUS segmentation, extracting tumor region from normal tissue regions of a BUS image, is a crucial step for a BUS CAD system. Base on the segmentation results, quantitative features will be extracted to describe tumor shape, size, orientation, echo pattern, etc., and be input into a classifier to determine the category of the tumors. Therefore, the precision of BUS segmentation directly affects the performance of the quantitative analysis and diagnosis of tumors.

Automatic BUS segmentation has been extensively studied in the last two decades. Due to the poor quality of BUS images, automatic BUS segmentation is a quite challenging task. We can

classify existing approaches into semi-automated and fully automated groups according to the degree of human intervention involved in segmentation process. In most semi-automated methods, user needs to specify a region of interest (ROI) including the lesion, a seed in the lesion, or initial boundary. Fully automated segmentation approaches need no user intervention, and usually model the knowledge of breast ultrasound and oncology as prior constraints for the segmentation. However, many segmentation techniques were employed in both semiautomatic and fully automatic approaches.

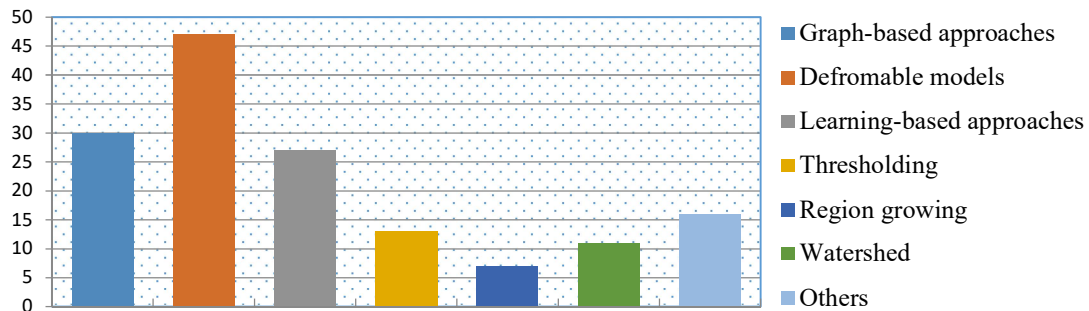


Fig. 1. Distribution of automatic BUS image segmentation approaches; data come from google scholar.

In this paper, we classify breast cancer segmentation approaches into six main categories: (1) graph-based approaches, (2) deformable models, (3) learning-based approaches, (4) thresholding, (5) region growing, and (6) watershed. As shown in Fig. 1, the first three categories dominate BUS image segmentation approaches; and the last three categories are the classical image processing approaches. The category of the others is composed of three small sub-categories, each contains only few literatures. Due to the challenging nature of the task, just using single image processing technique cannot achieve desirable results; and most successful approaches employ hybrid techniques and model biological priors.

The rest of the paper is organized as follows: in sections 2 - 5, we review automatic BUS image segmentation methods by presenting the principle of each category, discussing their advantages and disadvantages, and summarizing the most valuable strategies. In section 6, we discuss the approaches of three small sub-categories briefly. In section 7, the fundamental issues in BUS segmentation are discussed, e.g., denoising, interaction, biological priors modeling, validation, and the possible problem-solving strategies. Section 8 is the conclusion and the future directions.

2. Graph-based approaches

Graph-based approaches gain increasing popularity in BUS image segmentation because they offer several advantages: (1) they provide a simple way to organize task-related priors and image information in a unified framework; (2) they are flexible and suitable for expressing soft constraints between random variables; and (3) the computation based on graphical manipulation is very efficient [5].

Let $G = (\mathcal{V}, \mathcal{E})$ be a graph comprising a set of nodes (vertices) $\mathcal{V} = \{v_1, v_2, \dots, v_n\}$, and each of them corresponds to an image pixel or superpixel; and a set of links (edges) $\mathcal{E} = \{\langle v_i, v_j \rangle | v_i, v_j \in \mathcal{V}\}$, and each of them connects two adjacent nodes according to a predefined neighborhood system $\mathcal{N} = \{N_i | i = 1, \dots, n\}$ where N_i is the set of neighbors of node v_i .

Each link $\langle v_i, v_j \rangle$ is associated with a nonnegative weight $w(v_i, v_j)$. The weight is usually defined as the cost of separating the two connected nodes into different classes. The segmentation of an image is transferred to partition the graph into non-overlap subgraphs. The BUS segmentation is usually modeled as a bi-segmentation problem; therefore, the goal is to partition

graph G into two subgraphs (tumor and non-tumor). Let $G_A = (\mathcal{V}_A, \mathcal{E}_A)$ be the subgraph corresponding to non-tumor regions, and $G_B = (\mathcal{V}_B, \mathcal{E}_B)$ be the subgraph corresponding to the tumor regions, where $\mathcal{V}_A, \mathcal{V}_B \subseteq \mathcal{V}$ and $\mathcal{E}_A, \mathcal{E}_B \subseteq \mathcal{E}$, $\mathcal{V}_A \cup \mathcal{V}_B = \mathcal{V}$, $\mathcal{V}_A \cap \mathcal{V}_B = \emptyset$, and $\mathcal{E}_A \cap \mathcal{E}_B = \emptyset$.

2.1 MRF-MAP approaches

Markov random field (MRF) is a undirected graphical model, and provides a convenient way to model context-dependent entities (pixels or superpixels). In MRF, a site set $S = \{i\}_{i=1}^n$ is introduced to index the node set \mathcal{V} ; each site i is associated with a random variable X_i ; $x = \{x_i\}_{i=1}^n$ is the configuration (implementation) of random variable set $X = \{X_i\}_{i=1}^n$, and x_i takes value from a label set $\mathcal{L} = \{l_i\}_{i=1}^m$ where m is the number of labels (classes). In BUS image segmentation, the label set is usually defined as $\mathcal{L} = \{l_1, l_2\}$ where l_1 denotes tumor and l_2 denotes non-tumor.

Let $p(x)$ be the joint probability (also called the prior distribution) denoted as $p(X = x)$. X is said to be a MRF on S with respect to a neighborhood system \mathcal{N} if and only if it satisfies the positivity and Markovianity:

$$\begin{aligned} p(x) &= p(x_i | x_{S-\{i\}}) p(x_{S-\{i\}}) > 0 \\ &= p(x_i | x_{N_i}) p(x_{S-\{i\}}) \end{aligned} \quad (1)$$

where $x_{S-\{i\}}$ denotes a set of labels for sites $S - \{i\}$, and x_{N_i} is the set of labels for the neighboring sites of i .

Maximum a posteriori (MAP) is the most popular optimality criterion for MRF modeling and the optimal (x^*) is found by

$$x^* = \underset{x}{\operatorname{argmax}} p(x|d) = \underset{x}{\operatorname{argmax}} p(d|x)p(x) \quad (2)$$

where d is the observation (image), $p(x|d)$ is the posterior distribution and $p(d|x)$ is the likelihood distribution. The Hammersley-Clifford theorem [6] established the equivalence between MRF and Gibbs random field (GRF), and the MAP is equivalently found by minimizing the posterior energy function

$$x^* = \underset{x}{\operatorname{argmin}} E(x|d) = \underset{x}{\operatorname{argmin}} (E(d|x) + E(x)) \quad (3)$$

where $E(x|d) = E(d|x) + E(x)$, and $E(d|x)$ is the likelihood energy and $E(x)$ is prior energy.

There are two major parts in the MRF-MAP modeling for BUS image segmentation: (1) defining the prior and likelihood energies and determining the corresponding initial parameters; and (2) designing optimization algorithm for finding the minimum of the posterior energy.

Ashton and Parker [7] define the MRF prior energy as the Ising/Potts model

$$E(x) = \sum_{i \in S} V(x_i) + \sum_{i \in S} \sum_{j \in N_i} V(x_i, x_j) \quad (4)$$

$$V(x_i, x_j) = \begin{cases} \beta, & \text{if } x_i = x_j \\ -\beta, & \text{otherwise} \end{cases} \quad (5)$$

where β is a positive constant. The assumption that every site s takes any label equally likely makes $V(x_i)$ a constant for all configurations; therefore, $E(x)$ is usually defined on the pairwise term ($V(x_i, x_j)$).

They also assume that the intensities of a low-pass filtered image follow the Gaussian distribution, and the likelihood energy is given by

$$E(d|x) = \sum_{i \in S} \left[\ln(\delta_i^{x_i}) + \frac{(d_i - \mu_i^{x_i})^2}{2(\delta_i^{x_i})^2} \right] \quad (6)$$

where d_i is the intensity of the pixel at site i , x_i is the label of site i , and μ_{x_i} and δ_{x_i} are the local class mean and standard deviation, respectively. The parameters ($\mu_i^{x_i}$ and $\delta_i^{x_i}$) are estimated by

using a modified adaptive k-mean method [8] which estimates the class mean locally using a sliding window.

Boukerroui et al. [9] stated that healthy and pathological breast tissues present different textures of BUS images, and improved the method in [7] by modeling both intensity and texture distributions in the likelihood energy; they also assume that the texture features represented by using co-occurrence matrix follow the Gaussian distribution; and the parameters were estimated similarly to the method in [7].

To improve the additivity of BUS image segmentation method, Boukerroui et al. [10] modified the method in [9] by introducing a weighting function considering both global and local statistics. The weighting function is defined on the Kolmogorov-Smirnov distance between the global intensity distribution of the entire sites of a class and the distribution of the sites of the same class in a local window.

In [11], the proposed method followed the MRF-MAP framework, and formulated the BUS segmentation similar to [7], the only difference is that the Gaussian parameters are defined globally and specified manually. In order to improve the process of manual selection of Gaussian parameters in [11], reference [12] proposed a one-click user interaction to estimate Gaussian parameters automatically. The user specified only one pixel in tumor and the method opens a small window and a large window to obtain the lesion and background information, respectively. The foreground and background parameters were estimated using the pixel intensity distributions in the small and large windows. However, how to decide the window sizes was not discussed. [13] introduced the tissue

stiffness information of ultrasound elastography to the method in [11] by modifying the one-dimensional tumor and background Gaussian distributions as bivariate Gaussian distributions; however, it did not discuss how to determine the Gaussian parameters.

The energy function of MRF-MAP can be optimized by using Simulated Annealing (SA) [14] and Iterated Conditional Mode (ICM) [15] algorithms. Because ICM is much faster than SA, the ICM is preferred in most BUS image segmentation approaches [7, 9, 11 - 13]. ICM takes a local greedy strategy: it starts with an initial labeling from estimation or user interaction, then selects label for each site to minimize the energy function; and the steps repeat until converge.

ICM is quite sensitive to the initialization (parameters) because of its high possibility of converging to local minima, especially, for non-convex energies in high-dimensional space [35]. A detailed comparison between ICM and other MRF energy minimization techniques can be found in [35]. Therefore, one important issue of applying ICM is how to learn the parameters: Gibbsian parameter β (Eq. 6), number of classes (m), and parameters of the initial Gaussian distribution. The number of classes is usually set from 2 to 4 for BUS image; and β could be set adaptively [7] or set to a constant [11-13]; and the parameters of Gaussian distribution are usually initialized by using K-means algorithm [7, 9, 10].

2.2 Graph cuts

Graph cuts was proposed to solve a special case in MRF-MAP framework [16]: the global optimization of the binary labelling problem ($\mathcal{L} = \{l_1, l_2\}$). It was then improved to solve the general (color image segmentation) and multi-label problem [17, 18]. Graph cuts has been widely applied

to image segmentation. In this section, we will present the basic concepts of graph cuts, and review the approaches utilizing graph cuts for BUS image segmentation.

The main idea of graph cuts is to employ the theories and algorithms of the min-cut (s - t cut) and max-flow for binary segmentation. The graph G^{gc} is defined as following.

$$G^{gc} = (\mathcal{V}^{gc}, \mathcal{E}^{gc}), \mathcal{V}^{gc} = \mathcal{V} \cup \{s, t\},$$

$$\mathcal{E}^{gc} = \underbrace{\mathcal{E}}_{n\text{-links}} \cup \underbrace{\{\langle v, s \rangle | v \in \mathcal{V}\} \cup \{\langle v, t \rangle | v \in \mathcal{V}\}}_{t\text{-links}} \quad (7)$$

As shown in Eq. (7), graph cuts introduces two auxiliary nodes s and t representing the source and sink, respectively; the newly added edges between each node in \mathcal{V} and the terminal nodes (s and t) are called the t -links, and the original edges among neighboring nodes in \mathcal{E} are called the n -links.

A cut (C^{gc}) of G^{gc} is defined by

$$C^{gc} = \{\langle v_i, v_j \rangle | \langle v_i, v_j \rangle \in G^{gc} \text{ and } x_i \neq x_j\} \quad (8)$$

where x_i and x_j are the labels for nodes v_i and v_j , respectively; and the default labels for nodes s and t are l_1 and l_2 , respectively. The cost of the cut C^{gc} is given by

$$E(C^{gc}) = \sum_{\langle v_i, v_j \rangle \in C^{gc}} w(v_i, v_j)$$

$$= \underbrace{\sum_{v_i \in \mathcal{V}} x_i \cdot w(v_i, t) + (1 - x_i)w(v_i, s)}_{\text{data term}} + \beta \underbrace{\sum_{v_i \in \mathcal{V}, v_j \in N_i} (x_i - x_j)^2 w(v_i, v_j)}_{\text{smoothness term}} \quad (9)$$

In Eq. (9), w defines the weight of edge in \mathcal{E}^{gc} ; the cost function of a cut can be decomposed into two terms: the data term and the smoothness term. The data term is similar to the likelihood energy of MAP-MRF, which is usually modeled based on domain related knowledge (e.g., color

distribution, shape and location); and the smoothness term is usually to penalize the discontinuity between neighboring nodes. The segmentation of an image is to find a cut that minimizes $E(C^{g^c})$; the minimum s - t cut is equivalent to maximize the flow (max-flow) from s to t according to the Ford-Fulkerson theorem [19]. If a cost function is submodular [20], it can be represented by a graph (G^{g^c}), and the function can be minimized by using the max-flow algorithm. The Boykov-Kolmogorov version [21] of the implementation of the max-flow algorithm can be downloaded from <http://vision.csd.uwo.ca/code/>.

By applying graph cuts for BUS image segmentation, the key issue is how to define the data term and smoothness term. Xian et al. [22] proposed a fully automatic BUS image segmentation framework in which the cost function modeled the information in the frequency and space domains. The data term modeled the tumor pose, position and intensity distribution; and the weights are given by

$$w(v_i, t) = -\log[G(i) \cdot \Pr(d_i|x_i = 1)] \quad (10)$$

$$w(v_i, s) = -\log[(1 - G(i)) \cdot \Pr(d_i|x_i = 0)] \quad (11)$$

$G(i)$ is a 2D elliptical Gaussian function to model the tumor pose and position, and is constructed based on the results of the ROI generation [22]. $\Pr(d_i|x_i)$ defines the intensity distributions of the tumor and non-tumor regions.

The smoothness term is constructed based on the intensity discontinuities in the space domain and the edge detection results in the frequency domain; and the weight function is defined by

$$w(v_i, v_j) = (1 - ED(v_i, v_j)) + e^{-(d_i - d_j)^2 / 2\delta^2} / D_e(v_i, v_j) \quad (12)$$

where ED is the edge detector defined in the frequency domain, and D_e is the Euclidean distance between two nodes. For details, please refer [22, 23].

In [24], the graph is built on image regions, and user needs to specify a group of foreground (tumor) regions (F) and a group of background regions (B) to initialize the graph. The weight of any t-link is set to ∞ if the node belongs to $F \cap B$, and all other weights of t-links are set to 0; the weight function of the smoothness term is defined by utilizing region intensity difference and edge strength [138].

In [25], a discriminative graph cut was proposed, in which $w(v_i, t)$ and $w(v_i, s)$ in the data term were determined online by training a Probabilistic Boosting Tree (PBT) [26] classifier based on the detection results (foreground and background patches); and $w(v_i, v_j)$ in the smoothness term was learned offline utilizing the training set by the PBT. Hao et al. [27] constructed a hierarchical multiscale superpixel classification framework to define the weights in the data term. The hierarchical classifier has four layers (20, 50, 200, and 800 superpixels/nodes, respectively) built by using the normalized cut and k-means for multiscale representation; and a SVM classifier for each layer was trained based on superpixel histogram, position, shape clues, SGLD features and dense SIFT descriptor. The histogram difference (Euclidean distance) between adjacent superpixels was used to define the weights in the smoothness term. In [28], both the region-level [29] and pixel-level features were utilized to define the weights in the data term; and all weights were learned by using a structural SVM [30].

2.3 Normalized cut

In $E(C^{gc})$, the smoothness term is also called the length regularizer, and the minimization of $E(C^{gc})$ will cause the bias to favor small component (“shrinking” problem). To avoid bias, Shi et al. [31] proposed the Normalized cut to reformulate the energy function by considering both the disconnected links and the links inside each component:

$$\begin{aligned} Ncut(G_A, G_B) &= \frac{E(G_A, G_B)}{E(G_A, G_B) + E(G_A)} + \frac{E(G_A, G_B)}{E(G_A, G_B) + E(G_B)} \\ &= \frac{\sum_{(x_i=l_1, x_j=l_2)} w_{ij}}{\sum_{x_i=l_1} \sum_j w_{ij}} + \frac{\sum_{(x_i=l_2, x_j=l_1)} w_{ij}}{\sum_{x_i=l_2} \sum_j w_{ij}} \end{aligned} \quad (13)$$

where $G_A = (\mathcal{V}_A, \mathcal{E}_A)$ and $G_B = (\mathcal{V}_B, \mathcal{E}_B)$ are two subgraphs where $\mathcal{V}_A, \mathcal{V}_B \subseteq \mathcal{V}$ and $\mathcal{E}_A, \mathcal{E}_B \subseteq \mathcal{E}$, $\mathcal{V}_A \cup \mathcal{V}_B = \mathcal{V}$, $\mathcal{V}_A \cap \mathcal{V}_B = \emptyset$, and $\mathcal{E}_A \cap \mathcal{E}_B = \emptyset$; $E(G_A, G_B)$ is the total weight of the links between G_A and G_B ; $E(G_A)$ and $E(G_B)$ are the total weights in G_A and G_B , respectively; with this definition, the cut with small component will have small $E(G_A)$ or $E(G_B)$ and large $NCut$ value. The minimization of Eq. (14) can be transferred to the solution of the eigenvalue system if the equation is rewritten in the matrix form as following:

$$\begin{aligned} \min_x Ncut(G_A, G_B) &= \min_y \frac{y^T (\mathbf{D} - \mathbf{W}) y}{y^T \mathbf{D} y} \\ \text{s. t. } y^T \mathbf{D} \mathbf{1} &= 0 \text{ and } y_i \in \{1, -b\} \end{aligned} \quad (14)$$

where \mathbf{D} is an $n \times n$ diagonal matrix with $(\sum_j w_{ij})_{i=1}^n$ on its diagonal, and the weight matrix $\mathbf{W} = [w_{ij}]_{n \times n}$ is a symmetrical matrix; vector y is set as $(1 + x) - b(1 - x)$, and b is defined as $\sum_{x_i > 0} \sum_j w_{ij} / (\sum_{i,j} w_{ij} - \sum_{x_i > 0} \sum_j w_{ij})$. To make the equation tractable, the constraint is relaxed to allow y_i take real values; and the eigenvector with the second smallest eigenvalue of the *Laplacian* matrix $(\mathbf{D} - \mathbf{W})$ is the solution of the relaxed equation. Once the eigenvector with the second smallest eigenvalue is computed, one can bipartition the graph by choosing a split point of the

eigenvector (two-way cut). A recursive implementation of Normalized cut was proposed [31], which repeated the bipartition step on subgraphs until certain criterion is satisfied.

Generally, three main steps are for applying Normalized Cut to BUS image segmentation: (1) constructing a weighted graph (pixel-level or superpixel-level) to define the weight matrix (\mathbf{W}); (2) solving the Laplacian matrix ($\mathbf{D}-\mathbf{W}$) to obtain the eigenvectors, and applying the two-way cut or k -way cut to partition BUS image; and (3) determining the final tumor region by user interaction or formulated prior knowledge.

[27, 34] applied normalized cut as an initial step to segment BUS images into small patches, and the final segmentation needs extra merging step and formulated knowledge to determine the tumor region. Gao et al. [32] stated that traditional edge-driven approaches are too sensitive to noise and heavily depend on image denoising. [33] proposed a semi-automatic BUS image segmentation method based on Normalized cut. The feature of each pixel is defined using homogeneous patches, and weight (w_{ij}) between two nodes was defined as the similarity. Manual determination of ROI was needed in the segmentation, and the number of classes in the Normalized Cut was set as 2.

2.4 Summary

Graph-based approaches account for the second largest portion of BUS image segmentation literatures (Fig. 1). They are among the earliest techniques for BUS image segmentation, fade away due to the successful application of other powerful approaches such as deformable models (section 3),

and surge again because of the dramatic advances of graph models and energy optimization algorithms.

MRF-MAP-ICM is a flexible framework for image multi-partition (not just tumor or non-tumor). Most BUS image segmentation approaches based on this framework achieving good performance by designing better likelihood energy and obtaining better initialization. Only obtaining locally optimal solution is the main shortcoming of these approaches. Graph cuts provides an efficient framework for image bi-partition and MRF energy global optimization, and is the main factor to make graph-based models popular again in BUS image segmentation. The approaches based on graph cuts focus on designing more comprehensive data and smoothness terms to deal with low contrast, inhomogeneity, and not well-defined boundary problems of BUS images. The “shrink” problem is the common disadvantage of these approaches, and the extension [18] can only find the approximate solution of multiple labeling of graph cuts. Normalized cut avoids the “shrink” problem by considering both the disconnected links and the links inside each component. However, without the likelihood energy or data term, it cannot integrate semantic information into the energy, and usually needs user interaction or combining with other approach to achieve good performance; high computational cost is another drawback of Normalized cut. A detailed comparison of nine typical graph-based BUS image segmentation approaches is listed in Table 1.

As illustrated in Table 1, two approaches [25, 28] learned all parameters of graph models by using discriminative learning. This strategy enhances the robustness of graph models. Another potentially useful strategy is to build high-order graph models, in which every pair of nodes in the

graph has an edge; it can be applied to represent the global correlation among nodes, and can obtain a more representative smoothness term. The traditional algorithms such as ICM and max-flow cannot solve the high-order graph model effectively, and an efficient approach to optimize the fully connected graph model was proposed in [36].

Table 1. Comparison of graph-based approaches

Ref. / year	Category	F/S	Dataset	Useful Strategies	Disadvantages
[9], 1998	MRF- MAP-ICM	S	Qualitative	Integrate texture distribution; estimate distribution parameters locally	Depend heavily on parameters estimation; assume the Gaussian distribution of features
[11], 2002	MRF- MAP-ICM	S	Qualitative	Estimate distortion and segment image simultaneously	User interaction to set parameters; assume the Gaussian distribution of features
[10], 2003	MRF- MAP-ICM	S	Qualitative	Introduce the distance between global and local statistics to improve the adaptivity	Assume the Gaussian distribution of features
[13], 2016	MRF- MAP-ICM	S	33 images	Integrate tissue stiffness information from ultrasound elastography	Assume the Gaussian distribution of features
[23], 2015	Graph cuts	F	184 images	No distribution assumption; model the tumor pose, position; construct smoothness term in both spatial and frequency domains	“shrink” problem
[24], 2010	Graph cuts	S	13 images	Graph cuts on regions	User interaction to set the foreground and background priors; “shrink” problem
[25], 2010	Graph cuts	F	347 images	Learn the data and smoothness terms from images using deterministic model	“shrink” problem
[28], 2013	Graph cuts	F	469 images	Integrate features of superpixel and detection windows into the data term; learn all model parameters by using structured support vector machine [30]	“shrink” problem
[32], 2012	Normalized cut	S	100 images	No shrink problem	Manually select ROI

F denotes fully automatic approach and S denotes semi-automatic approach in Tables 1, 3 and 4.

3. Deformable models

Deformable models (DMs) are curves or surfaces that can move toward to the object boundary under the influence of *forces* defined on the curve or surface by using the knowledge of image. DMs can deal with biological structures with significant variability, and permit user to integrate expertise to guide the segmentation when necessary; therefore, they have been applied to BUS image segmentation extensively in the last decade.

DMs are proposed by Terzopoulos [37], and then become a popular and active field after the *snake* approach for planar image proposed by Kass et al. [38]. Generally, DMs can be classified into two categories according to the curve or surface representation during deformation: (1) the parametric DMs (PDMs) and (2) the geometric DMs (GDMs). In PDMs, curve or surface is represented by its parametric form explicitly, e.g., curve C is defined as $\{(x(p), y(p)) \mid p \in [0, 1]\}$ where $(x(p), y(p))$ is the coordinates of point p on C . The representation is intuitive and can lead to a fast implementation. GDMs represent curves and surfaces implicitly as a level set of a scalar function, e.g., $C = \{(x, y) \mid \phi(x, y) = 0\}$. It can adapt to topological changes of targets, which is helpful for segmenting multi-objects and objects with unknown topology.

3.1 Parametric deformable models

Finding object boundaries (parameterized curves and surfaces) using PDMs is formulated to minimize an energy function including *internal* and *external energies*. The internal term is used to control the continuity and smoothness of curves and surfaces; and the external energy function is calculated using image features to attract curves to object boundary.

Let $C(p) = (x_1(p), x_2(p)), p \in [0, 1]$ be a deformable curve; it moves to the optimal object boundary by minimizing

$$\mathcal{E}(C) = \mathcal{E}_{internal}(C) + \mathcal{E}_{external}(C). \quad (15)$$

The internal energy is defined by

$$\mathcal{E}_{internal}(C) = \frac{1}{2} \int_0^1 (\alpha \cdot (C')^2 + \beta \cdot (C'')^2) dp \quad (16)$$

where C' indicates the first order derivative of C that *keeps the continuity of curve*, and C'' is the second order derivative that *controls the smoothness of curve*; α and β are the weights; large α will lead the change in distances between points on curve to have high cost, and large β will penalize more on non-smooth curve.

The external energy is defined as the integral of a cost function based on image features along curve C :

$$\mathcal{E}_{external}(C) = \int_0^1 P(C(p)) dp \quad (17)$$

where P is the cost function based on image features. The general formulation of P in the original DMs [38] is defined by

$$P(x, y) = w_{line}P_{line}(x, y) + w_{edge}P_{edge}(x, y) + w_{term}P_{term}(x, y) \quad (18)$$

where P_{line}, P_{edge} and P_{term} extract image line, edge and termination features, respectively; while w_{line}, w_{edge} and w_{term} are the corresponding weights.

Minimization: the problem of finding the curve C minimizing $\mathcal{E}(C)$ is to find the extrema of functional which satisfies Euler-Lagrange equation [38]:

$$\frac{\delta \mathcal{E}(C)}{\delta C} = -\alpha(C'') + \beta(C''') + \nabla P = 0 \quad (19)$$

Table 2. Variants of PDMs

Categories	New External Forces	Pros	Cons
Gradient Vector Flow (GVF) [70]	$F_{ext}^* = v$, where v is the vector of GVF field	Relatively free of the initial contour; can deal with concave boundaries	Difficult to set the blending parameter; strong and weak edges create similar flow; cannot deal with topological changes
Balloon model [39]	$F_{ext}^* = F_{ext} + k\vec{n}$ \vec{n} is the unit vector to the curve, and k is the amplitude	Increased attraction range; can find the minima even the initial contour is smaller than the minima contour; limited to extract 2D curve	Cannot handle concave boundary; difficult to set the strength of the pressure; apply the issue of ignoring weak edges; cannot deal with topological changes
Distance map [146] and Balloon model [39]	$F_{ext}^* = k_1 \frac{-\nabla P}{\ \nabla P\ } + k\vec{n} + \nabla[e^{-d}]$ d defines the distance map calculating the distance between each pixel and its closest edge; k_1 is the weight	Normalized the external force F_{ext} to give more stable results; Increased attraction range; extended to extract 3D surface	Cannot handle concave boundary; cannot deal with topological changes

The above equation states that the functional derivative vanishes at the optimal curve. Given an initial curve C^0 , we can apply the gradient descent minimization to optimize $\mathcal{E}(C)$ iteratively. At step $t + 1$, the p th point on curve C is updated as

$$C^{t+1}(p) = C^t(p) + \gamma F(C^t(p)) \quad (20)$$

where γ is the step size, F is the force on curve defined as the negative of the functional derivative

$$F = \underbrace{\alpha(C'') - \beta(C''')}_{F_{int}} \underbrace{-\nabla P}_{F_{ext}} \quad (21)$$

where the internal forces F_{int} discourage curve stretching and bending, and the external forces F_{ext} often are composed of multiple forces to make the models flexible enough to handle different tasks.

The default PDMs discussed above may converge poorly for real image segmentation tasks because of several limitations, e.g., failing to converge to concave boundaries, and poor performance if the initial curve is not close to the minimum. Several variants have been proposed to address the problems of the default PDMs by introducing different external energy (Table 2).

3.2 Geometric deformable models (GDMs)

GDMs [40, 41] are proposed to overcome the two primary limitations of PDMs: lack of topology adaptivity and parameterization dependence. In GDMs, a 2D curve (C) at time t is represented implicitly as the *zero-level set* of a scalar function (ϕ): $C^t = \{C(p, t) = (x, y) | \phi(x, y, t) = 0\}$, and the curve deformation utilizes curve's geometric measures such as the unit norm and curvature, and image properties.

Let $\vec{v}(p, t)$ and $\vec{n}(p, t)$ be the speed and the unit normal vector of the p th point of an evolving curve at time t , respectively; the partial derivative of C with respect to t can be defined as the normal component of \vec{v} :

$$\frac{\partial C}{\partial t} = \vec{v} \cdot \vec{n}, \quad (22)$$

since the tangential component does not affect the geometry of an evolving curve.

Because of the curve representation by using level set function in GDMs, the deformation of curve is realized by evolving the level set function rather than tracking the evolution of the curve, which enables the *automatic topology adaption* of the embedded curve. Given a level set function $\phi(x, y, t)$, and a curve $\{C(p, t)\}$, we have

$$\phi(C(p, t), t) = 0, \text{ and } \frac{\partial \phi}{\partial t} + \nabla \phi \frac{\partial \phi}{\partial t} = 0 \quad (23)$$

If ϕ is negative inside and positive outside, the inside-pointing unit norm can be defined as $\vec{n} = -\frac{\nabla\phi}{|\nabla\phi|}$, and we can obtain

$$\frac{\partial\phi}{\partial t} = -\nabla\phi \cdot \vec{v} \cdot \vec{n} = \vec{v} \cdot |\nabla\phi| \quad (24)$$

Notice that the speed function \vec{v} is the key of GDMs; and it is usually defined as a function of the curvature (κ); to avoid the final curve shrinking to a point, image related information such as gradient is usually formulated to slow down the evolving process and to attract the evolving curve to the desired boundary.

Three important issues need to consider in GDMs implementation:

(1) designing the speed function. The foremost step in applying GDM is to design an appropriate speed function that can stop the evolving curve at the desirable object contour. A commonly used speed function is formulated as [42-44]

$$\vec{v} = g \cdot (V_0 + \kappa) - \langle \nabla g, \vec{n} \rangle \quad (25)$$

$$g = \frac{1}{1 + |\nabla(G_\sigma * I)|} \quad (26)$$

where V_0 is a constant to speed up the curve deformation, g is the stopping function by using image gradient to slow down and to stop the curve evolving at high gradient locations, and the second term ($\langle \nabla g, \vec{n} \rangle$) makes the stopping power stronger when there are no perfect edges.

(2) Initializing the level set function; the initial level set function is usually the signed distance from each point to the zero level set. A fast computation approach is described in [41].

(3) Reinitializing the level set function; the speed function is defined only on the zero level set; the level function deformation requires it to be extended to all level sets; the extensions [45] can cause

the irregularity problem of level set function. The reinitialization is applied to provide a numerical approach to replace the level set function with newly signed distance functions. For more information about the reinitialization, please refer [45-47].

3.3 Edge-based vs. Region-based DMs

DMs provide a flexible image segmentation framework that can incorporate both low-level image features and various prior knowledge, such as edge, local region statistics, shape, and intensity distribution. The DMs can be classified into edge-based [38, 41, 42, 44, 48] and region-based [47, 49, 66] according to the information to construct the external force in PDMs or speed function in GDMs. Edge-based DMs aim to attract the evolving curve to object boundary by defining the deformation force or speed using image gradient [42-44], and the models depend on image gradient to stop curve deformation. Region-based DMs model region features to guide the curve deformation; by modeling local region features, region-based models can usually achieve better performance than edge-based models; specially, if images have plenty of noise and weak object boundary.

3.4 Deformable models for BUS image segmentation

The application of DMs for BUS image segmentation can be divided into two stages. *In the first stage* BUS image segmentation approaches apply the ideas of PDMs, and focus on developing method to generate good initialization. To achieve global deformation and local variation of irregular tumor, Chen et al. [50] applied the B-snake model [51] for BUS image sequence segmentation. The external forces are composed of the balloon force and the second gradient of Gaussian smoothed image. No quantitative result was reported. In [52], Chen et al. proposed a cell-based

dual snake [53] to handle the two problems of applying traditional DMs for BUS image segmentation: (1) initial contour should be placed close to the tumor boundary; and (2) cannot capture highly winding tumor boundary. The attraction force between the inner and outer snakes makes the dual snake model escape from the local minimum. Qualitative evaluation has been conducted on both synthetic and real ultrasound images, but no quantitative result was reported. In [54, 55], Madabhushi et al. proposed a fully automatic approach for BUS image segmentation using PDM which is initialized by utilizing the boundary points produced in tumor localization step; and the balloon forces are employed in the external forces. The approach was evaluated by employing 90 BUS images with TP = 75%, FP = 20%, FN = 25%, HE = 19.7 and ME = 6.8.

In [56, 57], Sahiner applied PDM for 3D BUS tumor segmentation, the external forces have two terms; the first term is defined on image gradient calculated using 3×3 Sobel filters; and the second term is the balloon force. They evaluated the approach using the final tumor classification results of 102 BUS images.

In [58, 59], Chang et al. applied DM for 3D breast ultrasound image segmentation. The sticks filter [60] was utilized to enhance edge and reduce speckle noise. They evaluated the approach using eight 3D BUS cases, and the match rate was utilized for quantitative evaluation and the average is about 95%. Huang et al. [61] proposed an automatic BUS image segmentation approach by using the gradient vector flow (GVF) model [70]. The initial boundary was obtained by using Watershed approach. The approach was validated using 20 BUS images with similarity index = 0.884, overlap fraction = 0.81, and extra fraction = 0.058. Yap et al. [62] proposed a fully automatic

approach by applying GVF model. In its initial contour generation step, a fixed threshold was employed for candidate generation. The rules based on segment size and each segment's distance to the predefined reference point (RP) were applied to determine the initial tumor region. Totally 360 BUS images were utilized, but no quantitative results reported.

In the second stage, many works modified DMs to improve segmentation performance. Yezzi et al. [42] modified traditional GDMs to have an additional term ($\langle \nabla g, \vec{n} \rangle$) that provided stronger stopping power at object edges. Deng et al. [63] proposed a fast GDM method for biomedical image segmentation. The computation cost is linearly proportional to the number of image pixels. They only update the speed function and evolve the level set functions in a small window. The experimental results showed that it was much faster than the narrow band algorithm [52]. Liu et al. [64] proposed a fully automatic BUS image segmentation based on texture classification and GDM. The approach has two steps: the first step generated candidate tumor regions by using a well-trained texture classifier (SVM) to classify image lattices (16×16) into normal tissue and tumor, and a probability distance-based GDMs approach was proposed to find the final tumor boundary. The method was validated using 103 BUS images.

Gomez et al. [65] stated that GDMs establish stopping term based on image gradient may not work well because of the noisy and weak boundary. They proposed a BUS image segmentation approach based on the active contour without edges (ACWE) model [66] which defined the stopping term using Mumford-Shah technique and was robust to segment images with weak boundaries.

The initial contour is a five-pixel radius circle centered at a point in the tumor marked by user. They evaluated the approach using 50 BUS images.

Liu et al. [67] proposed an interactive BUS image segmentation approach utilizing region-based GDMs, in which the probability density difference between the intensity distributions (tumor and background) and the estimated Rayleigh distribution are applied to enforce priors of intensity distribution. The approach was compared with two other GDM approaches [66, 68] using 79 BUS images. Rodtook et al. [69] modified the generalized GVF [70] approach based on a continuous force field analysis, and applied it to BUS image segmentation. Daoud et al. [71] considered the SNR and local intensity value as two important features for estimating tumor boundary, and built a two-fold termination criterion based on the two features in discrete dynamic DMs [72]. Gao et al. [73] proposed a level set approach for BUS image segmentation based on the method in [47] by redefining the edge-based stop function using phase congruency [74] which is invariant to intensity magnitude, and integrated GVF model into the level set framework.

Cai et al. [75] proposed phase-based DM in which the local region statistics [49] is introduced to solve the inhomogeneous intensity problem, and the phase-based edge indicator is used to replace the conventional gradient-based edge operator. Lin et al. [76] modified the local region-based level set approach [77] by using additional constrained energies centered at four markers specified by radiologist. [78] proposed a fully automatic robust region-based level set approach with contour points classification (low contrast class and high contrast class). Different points on the curve may have different energy functions determined by the proposed locally signed pressure force function.

For the points in the low contrast class, both the global and local region-based energies [66, 77] are used; while for the high contrast class, only the local region-based [77] energy is utilized. [79] adopted the region-based approach in [78], proposed a learning based approach (multivariate linear regression and support vector regression) to produce the parameters adaptively, and proved better performance using 481 BUS images. Yuan et al. [80] proposed a new level set based DM approach; the local divergence and a smoothing kernel were introduced to improve the speed function.

Kuo et al. [81, 82] proposed a semi-automatic approach for 3D BUS image segmentation. The approach utilized user interaction to generate the volume of interest (VOI), applied the radial-gradient index [83] to estimate the initial lesion boundary, and implemented the region-based DM [48, 49] iteratively to find the final contour. The stopping criterion was defined as $(\bar{I}_F^{t+1} - \bar{I}_F^t) - (\bar{I}_B^{t+1} - \bar{I}_B^t) = 0$ [84], where \bar{I}_F^t and \bar{I}_B^t were the mean intensities inside and outside the segmented regions at step t , respectively. The approach was validated using 98 3D BUS images.

3.5 Summary

Table 3. Comparison of BUS image segmentation approaches based on deformable models

Ref. / year	Category	F/S	Dataset	Useful Strategies	Disadvantages
[30], 2003	PDMs	F	90	Use the balloon force to increase the attraction range.	Fixed reference point; difficult to set the strength of the balloon force
[33] 2003	PDMs	F	8(3D)	Define the external force using local texture features	Validated only on a small dataset, and sensitive to initialization
[39], 2004	PDMS	S	102 (3D)	Use the balloon force to increase the attraction range.	No quantitative evaluation of the segmentation
[59], 2007	PDMS	F	360	Use GVF to extend the attraction range and to handle concave boundaries	Fixed threshold and reference point are applied for initial boundary generation; no quantitative evaluation
[69], 2009	PDMs	F	103	Use a well-trained texture classifier to detect tumor ROI	Predefined rules to exclude false classified regions

[85], 2010	GDMs	S	79	Model the difference between the regional intensity distribution and the estimated prior distribution	Slow; sensitive to initialization
[124], 2012	PDMs	S	20	Redefine the edge-based stopping function using phase information	Validated only on a small dataset; sensitive to noise
[139], 2013	GDMs	S	168	Use both local statistics and phase information to define the speed function; and handle weak boundary and inhomogeneity problems better	Slow
[148], 2013	GDMs	F	861	Region-based GDM and solve the inhomogeneity problem better	Slow and sensitive to initialization
[166], 2014	GDMs	S	98(3D)	Use Region-based GDM and handle inhomogeneity problem	Slow and need user interaction to extract VOI

DM is the most popular approach applied to BUS image segmentation. For PDMs, the explicit curve or surface representation allows direct model interaction and can lead to fast implementation. The results of most PDMs are sensitive to initialization, and different initial curve or surface may converge to different local minimal locations and lead to quite different results; consequently, many variants of PDMs extend the attraction range to avoid local minima. The curves or surfaces of PDMs do not split and merge during the deforming process, which makes PDMs unable to adapt to topological change and to segment multiple objects with single initialization. GDMs apply level set functions to represent curves and surfaces implicitly, and inspire great progress in the related fields. There are two advantages of GDMs: (1) they can allow shapes to change topology during the evolving process, which makes them suitable for segmenting multiple objects and time-varying objects; and (2) the numerical computation of the curve and surface propagation can be implemented without parameterizing the objects. GDMs transfer the n -dimensional curve and surface

deformation into $n+1$ -dimensional level set function, which needs to extend the speed function to all level set functions and increases the computational cost greatly.

Table 3 presents detailed comparison of 10 typical DMs-based BUS image segmentation approaches. Because of the two advantages, GDMs become more popular than traditional PDMs in BUS image segmentation; and most successful approaches focus on improving the performance of GDMs to deal with the weak boundary and inhomogeneity of BUS images. There are two useful strategies: (1) redefining the stopping function (g), and making it independent of image gradient; and (2) redesigning the speed function by using regional statistics.

4. Learning-based approaches

Image segmentation can also be viewed as a classification problem, classifying pixels or superpixels into different categories. Therefore, it is quite common to apply machine learning approaches to image segmentation tasks. Both supervised and unsupervised learning approaches have been employed. By applying the unsupervised methods, BUS image is first partitioned into disjoint regions, and then prior knowledge (location, size, appearance, etc.) is utilized to determine the final tumor region.

4.1 Unsupervised learning approaches

K-means and Fuzzy C-means (FCM) are two popular unsupervised learning (clustering) approaches. Because K-means can be viewed as a special case of FCM, we only present the theoretical background of FCM in this section.

FCM was proposed in [85] and improved in [86]. Let $D = \{d_1, \dots, d_n\}$ be a finite set of data (pixels or superpixels), $LCs = \{ct_i\}_{i=1}^C$ be a list of C cluster centers; and FCM partitions set D into C clusters by minimizing the following objective function:

$$\min_c \sum_{i=1}^n \sum_{j=1}^c (u_{ij})^m \|d_i - ct_j\|^2 \quad (27)$$

In Eq. (28), $u_{ij} \in [0,1]$ is the *membership* value representing the degree of data point x_i belonging to cluster ct_j , and is given by

$$u_{ij} = \frac{1}{\sum_{c=1}^C \left(\frac{\|d_i - ct_j\|}{\|d_i - ct_c\|} \right)^{\frac{2}{m-1}}} \quad (28)$$

where m ($m \in R$ and $m \geq 1$) is the *fuzzifier*, and determines the degree of cluster fuzziness; a large m leads fuzzier clusters (smaller u_{ij}); if $m = 1$, u_{ij} takes values 0 or 1, which implies a hard partition (K-means); and m is usually set to 2 if no domain knowledge is introduced. The cluster centers are computed on all data points and weighted by their membership values:

$$ct_j = \frac{\sum_{i=1}^n (u_{ij})^m d_i}{\sum_{i=1}^n (u_{ij})^m} \quad (29)$$

The objective function (Eq. (27)) is optimized iteratively to find the local minimum in two simple steps: (1) decide the number of clusters (C) and assign the initial membership values (u_{ij}); and (2) iteratively update the cluster centers (Eq. (29)) and the membership values (Eq. (28)) until the membership values' change between two iterations is less than a predefined threshold.

The main advantage of the FCM is that each data point can belong to every cluster with a corresponding membership value rather than just belong to one cluster as in K-means, and FCM

can achieve better performance for overlapped data points. However, like K-means, the FCM algorithm can only find the local minima and the results depend on the initialization. A detailed comparison of BUS image segmentation approaches based on K-means and FCM is listed in Table 4.

In [7, 9, 10], K-means was utilized to estimate the parameters of distributions in graph-based models, and the predefined number of clusters should be set. Xu et al. [87] proposed a BUS image segmentation method using the spatial FCM (sFCM) [88] with local texture and intensity features. In sFCM, the membership value of each point is updated by using its neighbors' membership values. The number of clusters (C) is set as 2, and the initial membership values are assigned by using the modes of image histogram. Lo et al. [89] applied FCM to generate image regions in four clusters, then extracted the morphology, location, and size features of each region; and finally trained a linear regression model [90] to produce the tumor likelihoods for all regions. The region with the highest likelihood is considered as a tumor. Moon et al. [91] applied FCM to image regions produced by using the mean shift method [92]; the number of clusters is set to 4, and the regions belonging to the darkest cluster are extracted as the tumor candidates. [91] trained a linear regression model to estimate the tumor likelihoods of candidate regions utilizing seven quantitative features which were extracted according to the American College of Radiology (ACR) Breast Imaging Reporting and Data System (BI-RADS) [93]. [89, 91] did not discuss how to initialize the membership values in FCM. To deal with the blur boundary and uncertainty in BUS images, Shan et al. [94, 95] extended the FCM and proposed the neutrosophic l-means (NLM) clustering which takes

the indeterminacy of membership into consideration, and can handle the uncertainty in BUS images much better.

4.2 Supervised learning approaches

4.2.1 Support vector machine (SVM)

SVM is one of the most popular supervised-learning models in machine learning, and can be utilized for both linear classification (linear SVM) and non-linear classification (kernel SVM) [96, 99] by mapping its inputs to high dimensional spaces.

Let $\{(d_i, x_i)\}_{i=1}^n$ be a training dataset of n points where x_i is either 1 or -1, indicating the class of data point d_i ; SVM aims to find a hyperplane which can separate the training samples by a gap as wide as possible. Let w be the normal vector to the hyperplane, and $\{\zeta_i = \max(0, 1 - x_i(w \cdot d_i + b))\}_{i=1}^n$ be slack variables for the soft margins; then the problem can be formulated as a constrained quadratic optimization problem [97]

$$\min \frac{1}{n} \sum_{i=1}^n \zeta_i + \lambda \|w\|^2 \quad (30)$$

$$s. t. \quad \forall i, x_i(d_i \cdot w + b) \geq 1 - \zeta_i \text{ and } \zeta_i \geq 0$$

Finally, w and b learned from the training dataset can be used to classify new data by computing $x_i = \text{sgn}(d_i \cdot w + b)$.

Liu et al. [98] trained a kernel SVM classifier [99] using the local image features to classify small image lattices (16×16) into tumor or non-tumor classes; the radius basis function (RBF) was

utilized; and 18 features, including 16 features from co-occurrence matrix and the mean and variance of the intensities, were extracted from a lattice; then some post-processing operations, like removing line-like areas and filling holes, were utilized to determine the final tumor regions.

Jiang et al. [100] proposed two-step BUS segmentation approach. First, a set of candidate tumor regions were produced by using Adaboost classifier [101] and 24 Haar-like features [102]; and a SVM classifier was trained using the quantized intensity features produced by K-means clustering to determine the false positive and true positive regions. Second, random walk [103] was applied to generate the final tumor boundary by placing seed at the center of each true region.

4.2.2 Artificial Neural network (ANN)

ANN is another popular supervised learning approach for BUS image segmentation. ANN mimics the biological neural networks, and is capable of approximating arbitrary function from observed data.

A typical ANN has three layers: an input layer, a hidden layer and an output layer, interconnected by weighted links, e.g., $w_j^I = [w_{1,j}^I, \dots, w_{n_I,j}^I]^T$ is the weight vector of the links between j th hidden units and the input units, and $w_k^O = [w_{1,k}^O, \dots, w_{n_I,k}^O]^T$ is the weight vector between the k th unit in the output layer and the hidden units. The units in the layers are usually called ‘neurons’. The input neurons represent the feature vector $x = [x_1, \dots, x_{n_I}]^T$; h_j is the output of the j th hidden neuron; and $z = [z_1, \dots, z_{n_O}]^T$ yielded in the output layers will be used for classification. The output of the k th neuron in the output layer (z_k) is

$$z_k = \varphi \left(\sum_{j=1}^{nh} w_{k,j}^o \cdot \varphi \left((w_j^i)^T \cdot x \right) \right) \quad (31)$$

where $\varphi(\cdot)$ is the activation function of a neuron (hidden and output layers), and converts a neuron's weighted input to its output value; the preferred activation function should be non-linear and differentiable such as the sigmoid and hyperbolic tangent functions.

The learning process of ANN is to determine the weights of all links using a set of training data. In practical situations, the mean-squared error (MSE) is commonly used as the cost function and the well-known backpropagation algorithm is for training ANNs.

Huang et al. [103] proposed an ANN-based method to segment 3D BUS images by processing 2D images slices. First, thresholding was applied to generate candidate regions; then five region features (average gray level intensity, entropy, ratio of region size to slice size, ratio of region size to the size of its bounding box, and the distance from the region center to image center), were used as the inputs of NN; furthermore, among all the slices, the image having a region with the highest NN output was set as the reference image in which the region was set as tumor region; the reference image and tumor region was compared with adjacent slices to find new tumor regions, which later was used as a new reference. The 3D boundary of BUS tumors was reconstructed after all image slices were processed. The number of hidden unites and output units was not discussed.

[104] trained an ANN to generate the threshold for BUS image segmentation. Two feature extraction approaches were proposed: 1) using $128 \times n_{key}$ SIFT features where n_{key} is the number of key points; 2) exacting 4 texture features (contrast, correlation, energy and homogeneity) of

40×40 region around each key point using GLCM along four directions, and the final dimension of the texture feature matrix is $16 \times n_{key}$. Therefore, the input feature vector is $144 \times n_{key}$. The ANN has 3 layers, 60 nodes in hidden nodes, one node in the output layer. The stop criterion is 10^{-7} of the MSE.

Shan et al. [105, 106] trained an ANN using three new features: the phase in the max-energy orientation (PMO) based on phase congruency, radial distance (RD) and the joint probability of intensity and texture [30]. The NN had 6 hidden units and 1 output unit.

4.2.3 Naive Bayesian classifiers (NBCs)

NBCs are a family of probabilistic classifiers based on the strong independence assumption: given the class variable, each feature is independent of other features in the feature vector. By using the strong independence assumption and the Bayes' theorem, the conditional distribution over the class variable is

$$p(x_k|d) = \frac{1}{Z} p(x_k) \prod_{i=1}^n p(d_i|x_k), k = 1, \dots, K \quad (32)$$

where $d = [d_1, \dots, d_n]^T$ is the variable of n independent features, and $x = [x_1, \dots, x_K]^T$ is K class labels; $Z = p(x)$ is a constant if the values of the feature variables are known; $p(x_k)$ is the prior distribution of label x_k .

NBC commonly combines the conditional distribution and the MAP decision rule to construct the classifier:

$$\hat{x} = \underset{x_k}{\operatorname{argmax}} p(x_k) \prod_{i=1}^n p(d_i|x_k) \quad (33)$$

Applying NBC, the first thing is to calculate the prior by assuming equiprobable classes ($p(l_k) = p(l_j), i \neq j$) or by estimating from the training set; and then one must assume the conditional distribution ($p(x_i|l_k)$) over feature variables or learn a nonparametric model from training set.

Yang et al. [138] proposed a whole breast tumor detection method by classifying slice pixels into tumor (x_1) or normal tissue (x_2) by using NBC. Two features, local (5×5 mask) intensity mean and stick filter [60] output, were utilized; the class priors were assumed to be equiprobable, and the conditional distribution of each feature (x_i) was assumed to be Rayleigh distribution:

$$p(x_i|l_k) = \frac{x_i}{\sigma_k} e^{-x_i^2/2\sigma_k^2}, k = 1, 2 \quad (34)$$

where σ_k is the Rayleigh parameter and can be estimated from training data. NBC produced a set of suspected lesions, and a two-phase lesion selection method based on region shape features (area size, width-height ratio, region ratio and compactness) and region continuity and volume size were applied for final tumor region decision [108].

Table 4. Comparison of learning-based BUS image segmentation approaches

Ref.	Category	F/S	Dataset	Advantages	Disadvantages
[7, 9, 10]	Adaptive K-means	S	Several images	Achieved better performance than the standard K-means on images with local intensity variations	Sensitive to initialization; only used for estimating distribution parameters
[89]	FCM	F	58 lesions (ABUS images)	High sensitive rate	Sensitive to initialization; high false positive rate
[91]	FCM	F	148 lesions (ABUS images)	High sensitive rate	Sensitive to initialization; used fixed threshold to merge regions
[98]	SVM	F	112 images	Utilized local texture features to classify local lattices and achieved high precision and recall ratio	Only produced rough tumor boundaries; depended on post processing rules to refine the results
[100]	SVM	F	112 images	Balanced sensitivity and specificity	Slow; depended on random walk to generate the final boundary

[103]	ANN	F	93 cases (3D)	Fully automatic	Depended on fixed threshold to produce candidate regions; relatively low performance
[106], 2012	ANN	F	120 images	Achieved good performance by using the phase information, radial distance and the joint distribution of texture and intensity	Depended on fixed reference point to generate the initial ROI
[107], 2012	NBC	F	31 cases (Whole BUS images)	Achieved high sensitive ratio	Depended on the assumption of intensity distribution; depended on post selection to reduce false positive ratio

4.3 Summary

Unsupervised learning is simple and fast, and has been widely utilized in many BUS image segmentation approaches. However, because of the challenging nature of BUS image segmentation, unsupervised approaches are only used as a preprocessing step to generate candidate image regions and more sophisticated methods are usually employed to perform the final segmentation; for example, in [7, 9, 10], K-means is utilized to estimate the initial parameters of intensity or texture distributions; and in [89, 91], logistic regression is utilized for clustering results to find the final tumor.

Supervised learning provides a good framework to integrate different levels of features and to learn knowledge between the inputs and target outputs. Many BUS image segmentation approaches achieve good performance by using supervised learning approaches. Most of them design features using domain knowledge (feature engineering) to improve the performance. They can be integrated with other segmentation techniques, e.g., in [25, 28], supervised learning approaches learn the parameters of the graph-based models from the training data; they also can be used to perform

segmentation alone, e.g., in [120], a well-trained ANN was applied to perform the tumor segmentation. One common disadvantage of the supervised learning approaches is that they cannot produce accurate tumor boundary, and refinement is usually necessary.

Learning-based approaches thrive in BUS image segmentation in the last decade and we believe new deep learning techniques [162] such as deep convolutional neural networks (CNNs) and recurrent neural network (RNN) will make great progress in segmenting BUS images in the near future.

5. Classical Approaches: thresholding, region growing and watershed

In this section, we will discuss some classical segmentation approaches applied to BUS image segmentation, and they are usually combined with other methods to achieve good performance.

5.1 Thresholding

Thresholding is the most intuitive, simple and fast segmentation approach, and enjoys popularity in BUS image segmentation. It groups image pixels directly into regions by using a single threshold (two classes) or multiple thresholds (multiple classes) based on pixel features (e.g., intensity, color, local mean, standard deviation, etc). A threshold th segments image pixels into two classes:

$$y(p) = \begin{cases} l_1, & \text{if } I(p) > th \\ l_2, & \text{if } I(p) \leq th \end{cases} \quad (35)$$

where $I(p)$ is the intensity of the p th pixel; and l_1 and l_2 are the labels for two classes. When th is a constant over entire image, the method is called *global thresholding*; if th is changing over the local features, the method is referred as *adaptive/local thresholding*. Global thresholding is fast and

works well when the intensity distributions of objects and background are sufficiently distinct; however, if the object-background contrast is low, image is noisy, and/or illumination varies across the image, global thresholding cannot achieve good performance. There are two solutions: (1) applying image enhancement techniques before global thresholding, and (2) using local thresholding method adaptively.

Thresholding is often used as a pre-segmentation step for tumor localization and the computational efficiency is more important than the accuracy; therefore, the pre-segmentation scheme of global thresholding with image enhancement is preferred.

There are three main approaches to select the global threshold. The first is to choose empirical value as the threshold for the whole dataset [109-111]; the second approach is to select the threshold for each image based on domain related rules [112, 113]; and the third is to generate the threshold automatically based on statistical-decision theory [22, 114, 115].

5.2 Region growing

Region growing extracts image regions from a set of pixels (*seeds*) and growing seeds to bigger regions utilizing predefined *growth criteria*.

Seed generation: the *seeds* can be placed by user interactively [116, 117] or generated automatically [54, 55, 113, 118]. In [54, 55], Madabhushi et al. selected seed (p^*) automatically from a set of candidate pixels by formulating empirical rules [55]:

$$p^* = \operatorname{argmax}_p \left(\frac{\Gamma(i_p, t_p) \cdot J_p \cdot Y_p}{d_p} \right) \quad (36)$$

where i_p and t_p are the intensity and texture values of pixel p , respectively; $\Gamma(i_p, t_p)$ is pixel p 's value of joint intensity and texture probability; J_p refers to the local mean value of Γ around p ; Y_p is the row position (origin at the lower-left of image) of p and avoids selecting seed from the shadowing region which appears in the bottom of BUS image; and d_p is the distance between p and image center. [118] used this method for seed generation. For each pixel p adjacent to the seed region, if p satisfies (growing criterion): $J_p/J_{p^*} \in [\beta_1, \beta_2]$, p will be added to the seed region, where β_1 and β_2 are selected by experiment. The growing process will stop until no more pixel satisfying the condition

Shan et al. [113] proposed another automatic seed generation approach. Thresholding was used to generate a group of candidate regions; and the region ranking criteria based on region location, size and local feature, were utilized to determine a true tumor region (r^*):

$$r^* = \operatorname{argmax}_r \left(\frac{\sqrt{A(r)}}{d_r \cdot \operatorname{var}(r_c)} \right) \quad (37)$$

where $A(r)$ is the number of pixels in region r ; d_r is the distance between the center of r and the fixed reference point (center of the top half of image); r_c is the center of region r ; and $\operatorname{var}(r_c)$ is the local variance of a circular region at the center of region r ; a pixel inside region r^* will be selected as the seed. Let $I(p)$ and $\bar{I}(p)$ be intensity and local mean intensity of pixel p , respectively, the growing criterion is defined by

$$\begin{aligned} 1 - e^{-\frac{\operatorname{var}(p)}{100}} \leq t_1 \quad \text{and} \quad 1 - \frac{|I(p) - m(r_s)|}{m(r_s)} \geq t_2 \quad \text{or} \\ 1 - e^{-\frac{\operatorname{var}(p)}{100}} \geq t_1 \quad \text{and} \quad 1 - \frac{|\bar{I}(p) - m(r_s)|}{m(r_s)} \geq t_3 \end{aligned} \quad (38)$$

where $m(r)$ is the average intensity of the current seed region, and t_1 , t_2 and t_3 are set as 0.5, 0.2 and 0.99, respectively. The growing processing stops when no more pixel satisfies the above condition.

Kwak et al. [117] defined the cost of growing a region by modelling common contour smoothness and region similarity (mean intensity and size):

$$J(r_s, r) = \frac{(m(r_s) - m(r)) \cdot A(r_s) \cdot A(r)}{\alpha \cdot LC(r_s, r) + \beta \cdot A(r_s) + A(r)}, r \in N(r_s) \quad (39)$$

where $m(\cdot)$ denotes the mean intensity of a region, $A(\cdot)$ is the pixel number of the region, $LC(r_s, r)$ is the length of the common contour between the seed region r_s and region r , $N(r_s)$ is a set of regions adjacent to r_s , and α and β are two predefined constants. The region with the minimum value of J will be added to the seed region. The growing will repeat until $\sum_{r \in N(r_s)} J(r_s, r)$ over the length of contour r_s reaches the maximum.

5.3 Watershed

Watershed is a powerful image segmentation method, and usually produces more stable results than thresholding and region growing approaches, and offers a framework to integrate domain-related priors as well. There are different definitions of watershed [119, 120]. The most popular definition is the *watershed by flooding* [119]; and the idea is to place a water source in each local minimum (*marker*), then flooding the image from the markers, and building barriers at the points of the first contact of different water sources. The barriers are the watershed and the boundaries of objects. The most common implementation of watershed for image segmentation can be found in [121]. In practice, watershed is usually applied to gradient image on which the pixels with small values in a catchment basin correspond to an object. The key issue in watershed segmentation is the *marker*

selection. One approach is to choose the local minimum gradient as the marker, which will usually result in over-segmentation due to noise, and further step such as region merging should be involved. The other approaches choose markers based on more complex predefined criteria that can utilize the task-related priors.

Huang et al. [122] applied the watershed to segment the preprocessed BUS images and the markers were selected based on grey level and connectivity. [109, 123] used watershed to segment ROI into small regions, and used the predefined criteria (area, mean intensity, geodesic center, etc) to determine the final tumor region. 255 groups of markers were selected by thresholding ($th = 1, 2, \dots, 255$) the image [124, 125]; the external and the internal markers were defined by using the morphological dilation and erosion. Watershed method was applied to generate 255 potential lesion boundaries by using the markers on different thresholds; the average radial derivative (ARD) function was applied to determine the final tumor boundary. Zhang et al. [126, 127] applied watershed to determine the boundaries of gray level images. The markers are set as the connected dark regions; and post processing based on predefined criteria (region location, mean intensity, and ratio of width to length) is needed to refine the results. [128] applied watershed to generate meaningful regions, and refined the regions by removing the top 50% hyper-echogenic (bright) regions and the regions connected to the image border to generate candidate tumor regions; the candidate regions were distinguished between tumors and non-tumors by using a logistic regression classifier [129] trained using region morphology, intensity and texture features.

5.4 Summary

Table 5. Comparison of classical approaches

Ref.	Category	Purpose	Threshold/Seed/Marker Generation	Additional Comments
[110, 111]	Global thresholding	Pre-segmentation	Fixed threshold	Depended on image enhancement; could not adapt to variations of image quality.
[113]	Global thresholding	Candidate tumor region generation	Iterative thresholding by finding the local minima of histogram.	Depended on post empirical rules to refine the candidate regions; used fixed reference position.
[115]	Global thresholding	ROI generation	Otsu's algorithm [130]	Depended on image preprocessing.
[55]	Region grow	Pre-segmentation	Selected seed by formulating empirical rules.	Used image center as the fixed reference position.
[117]	Region grow	Final segmentation	User interaction to set an elliptical seed region	Depended on image enhancement; the growth criteria were defined by formulating contour roughness and region inhomogeneity.
[122]	Watershed	Final segmentation	Selected marker by using intensity and connectivity	Depended on image enhancement.
[124]	Watershed	Pre-segmentation	Decided the external and internal markers by computing the Beucher gradient [131] of the morphological dilation and erosion of the binary image	Depended on image preprocessing; select 255 groups of markers by thresholding image using thresholds from 0 to 255; needed additional geometrical measure [132, 133] to decide the final tumor contour.
[127]	Watershed	Pre-segmentation	Used regions on the binary edge map as markers	Depended on empirical rules to refine the results
[128]	Watershed	Pre-segmentation	Local intensity minima	Depended on empirical rules to refine the results

In this section, we present the theoretic background of three classical image segmentation approaches: thresholding, region growing and Watershed; and discuss their applications to BUS image segmentation. The three approaches are quite simple, fast and efficient to conduct initial segmentation of BUS image, and facilitate further segmentation procedures. The most common purpose of applying these approaches is to locate tumor by generating candidate regions or boundaries, and to use the results to initialize further segmentation. These classical approaches usually use

simple low-level image features such as intensity and local statistics to perform segmentation, and are vulnerable to low image quality due to noise, inhomogeneity and low contrast. Therefore, to achieve good performance of BUS image segmentation, two additional steps are usually needed: first, image preprocessing step is applied to improve image quality by denoising and enhancing contrast; second, more delicate approaches are utilized to refine the segmentation results.

6. Other approaches

Beside the four main categories of BUS image segmentation approaches discussed in sections 2-5, there exist some interesting approaches presented in few papers. We discuss them briefly in this section.

Cellular automata (CA): CA was introduced by von Neumann [133] and applied to interactive image segmentation [134]. In image segmentation, a cell is usually associated with a pixel or superpixel. A CA is defined as a triplet $CA = (St, \mathcal{N}, \delta)$ where St is the state set, \mathcal{N} denotes the neighborhood system, and δ is the transition function which defines the rule of updating the cell state based on the states of the neighborhood cells at previous step. The Moore neighborhood (8-neighbor) and von Neumann neighborhood (4-neighbor) are two commonly used neighborhood systems in CA. Each element in the state set St has three components: the cell label (l_p), cell strength ($\theta_p \in [0, 1]$), and feature vector (V_p). The states of all cells are initialized as $(l_p, \theta_p, V_p) = (0, 0, V_p)$ where V_p can be initialized in different ways, e.g., the color vector or intensity of a pixel; when user specified seed cells, the strength values of the seed cells will be set to 1, and their labels will be set accordingly (e.g., 1 for foreground seed, and 0 for background seed). After the initialization, CA

will update the states of all cells according to the evaluation rule: let (l_p^t, θ_p^t, V_p) be the state of cell p at time step t , and the state of the cell at time step $t+1$ is defined by

$$(l_p^{t+1}, \theta_p^{t+1}, V_p) = \begin{cases} (l_q^t, \theta_q^t, V_p), & \text{if } T(p, q) \cdot \theta_q^t > \theta_p^t \\ (l_p^t, \theta_p^t, V_p), & \text{otherwise} \end{cases} \quad (40)$$

where cell q belongs to $\mathcal{N}(p)$, and $T(p, q) \in [0, 1]$ is the transition function usually defined on the similarity between V_p and V_q .

Liu et al. [135] constructed the transition function by integrating the global information on the transition chain and local texture correlation. The CA-based segmentation approaches are widely used for interactive segmentation and could achieve good performance of BUS image segmentation. There are three main advantages of CA-based approaches: (1) support multiple objects segmentation; (2) can generate very precise object boundary and does not have the “shrink” problem; and (3) support user input on the fly. These approaches usually start with user interaction to initialize the labels of seed cells, and then update the states of all other cells according to the evolution rule until all cells reach the stable states or the fixed number of iterations is reached. The procedures are simple and easy to implement, but two important issues have to be considered. First, CA-based approaches need accurate user interactions, and different initializations may lead to quite different segmentation results. Second, because all cells are visited during each iteration, therefore, the computation cost is high; especially, when the image size is large. For a fast CA-based segmentation approach, refer [137].

Cell competition: Chen et al. [138] proposed a cell-competition approach for BUS image segmentation. The cells are small image regions generated by using a two-pass Watershed segmentation;

and then adjacent cells compete to generate new regions by splitting or merging. There are two types of competitions. In Type I competition, two adjacent cells from different regions compete with each other; a cell may split from a region and merge into another region. In Type II competition, one cell splits from a multi-cell region and forms a single-cell region.

Chen et al. [138] applied the cell competition approach to partition manually selected image ROI into several regions, and to form the final tumor ROI by user interaction. Cheng et al. [139] applied the approach to an initial slice selected by user, and used the results to partition the cells of other slices into object or background regions. The two regions in each slice compete to find the tumor boundaries. Chiang et al. [140] extended the approach to segment 3D BUS image, and applied Graph cuts to image regions for finding the final tumor boundary. Cell competition approaches are designed to partition image into small regions, and no task-related knowledge is integrated in the competition mechanism. It is simple and fast, but needs large amount of user interactions to select ROI before the competition or to select tumor regions after the competition.

Radial gradient index (RGI): RGI is utility function (Eq. (41)) which was proposed in [141] to segment mammograms. It calculates around the boundary of each candidate partition, and the partition with the largest RGI value is selected as the tumor region.

$$RGI(\mathcal{M}_i) = \frac{1}{\sum_{p \in \mathcal{M}_i} |\nabla f(p)|} \sum_{p \in \mathcal{M}_i} \nabla f(p) \cdot \frac{\vec{r}(p)}{|\vec{r}(p)|} \quad (41)$$

In Eq. (42), \mathcal{M}_i is a set of contour points of the i th image partition; $|\nabla f(p)|$ is the absolute value of the intensity gradient at point p ; and $\vec{r}(p)$ is the radial vector point from the partition center to point p . The RGI value measures the proportion of the intensity gradients of the boundary

points along the radial direction. It takes values in $[-1, 1]$; RGI value 1 indicates that all the gradients point outward along the radial vector; and -1 signifies that all the gradients point inward along the radial vector. For actual BUS tumor regions, the RGI values are expected to close to 1.

Drukker et al. [142] applied RGI to perform tumor detection. The RGI value is calculated on a set of contours centered at each pixel, and the maximal RGI value of each pixel is used to replace pixel's intensity, which formed a RGI-filtered image; then thresholding was applied on the RGI-filtered image to determine a region of interest (ROI). In [142], the contour with max ARD value [25,26] was chosen as the final tumor contour. In [143, 144], a NN with five 5 hidden units was used to classify the candidate lesions into true positive and false positive; Kuo et al. [145, 146] applied RGI to find the initial tumor contour of 3D BUS image. The RGI calculation is simple and easy to implement; however, it calculates a group of RGI values for each pixel, and the computation cost is quite high; furthermore, it depends on image gradient, and cannot obtain accurate tumor boundary of BUS image due to low image quality.

7. Fundamental Issues of BUS Image Segmentation

Extensive BUS segmentation approaches have been studied in the last two decades, and many of them achieved good performances utilizing their own datasets. In this section, we discuss the fundamental issues in BUS segmentation, and summarize the successful strategies employed in state-of-the-art approaches.

7.1 Denoising and Preserving Edge

In ultrasound imaging, speckle noise is inherent to coherent illumination and Rayleigh scattering caused by tissue microstructures [147], and it is a major difficulty in BUS image segmentation. Many de-speckle approaches have been applied, e.g., mean filter, Gaussian low-pass filter, speckle reducing anisotropic diffusion (SRAD) [148], nonlinear coherence diffusion (NCD) [149], sticks filter [60], bilateral filter [150, 151], fractional subpixel diffusion [157], etc.

Mean filter and Gaussian low-pass filter are simple and fast, and widely used in early BUS segmentation approaches [22, 52, 61, 59, 62, 63, 109, 115, 112, 123, 133, 138]; SRAD, NCD, sticks filter, and fractional subpixel diffusion are specially designed to deal with speckle noise, and because of their excellent property in edge preservation, these approaches obtained popularity in BUS segmentation [34, 58, 65, 89, 95, 103, 105, 106, 113, 114, 124, 125, 158, 165, 166].

The mean filter and Gaussian low-pass filter have the side effect of blurring edges, and are only suitable for the approaches insensitive to image edges or gradient. For the edge-based approaches, e.g., edge-based DMs, watershed, and edge detection approaches, denoising with edge preservation approaches are preferred to avoid the leakage of final segmentation.

7.2 Human Intervention

Many semi-automatic approaches exist in literatures; user interactions like setting seeds, drawing initial boundary or ROI are required in these approaches. Radiologists' interaction could be useful in segmenting extremely difficult BUS cases which have very low image quality; however, these interactions make the approaches operator-dependent and the results unreproducible; furthermore, it is also impossible to apply the semi-automatic approaches to a large-scale BUS image dataset,

because of the great cost of human labor and time. The intensity and sensitivity of interaction are two important criteria for evaluating interactive segmentation approaches [152, 153]; because user interaction has large degree of arbitrariness and different interaction may lead to quite different results. However, no work has been done in BUS image segmentation to evaluate the approach's interaction sensitivity and intensity yet.

Fully automatic BUS image segmentation has many advantages in comparison with interactive segmentation, such as fully operator-independent, objective, and suitable for large scale tasks; hence, we believe that fully automatic segmentation is the trends in the future for BUS CAD systems. Many fully automatic approaches [22, 25, 64, 98, 100, 106, 109, 115] have been proposed in the last few years.

In fully automatic BUS segmentation, the key step to make an approach completely automatic is the tumor detection, which outputs ROI, rough boundary, seeds, or candidate regions to localize tumors, and initializes the subsequent segmentation steps. Ikedo et al. [109] determined tumor ROI by using vertical and horizontal edges detected by using the Canny edge detector. Liu et al. [64, 98] detected tumor ROI by using a well-trained texture classifier (SVM) to classify image lattices (16×16) into normal tissue and tumor. Zhang et al. [25] estimated the bounding box of tumor using a binary classifier trained by negative (normal tissues) and positive (tumor) patches. Jiang et al. [100] applied ensemble learning method (Adaboost) to generate a boosted classifier for locating candidate rectangular regions; then these regions were refined by a SVM to generate the final true regions. Shan et al. [106] formulated the texture, spatial location, and size of the candidate area to

rank the regions obtained from the iterative thresholding, and selected the center of the winning region as the seed. Xian et al. [22, 115] took advantage of the layer structure of BUS image, and proposed the adaptive reference position (RP) generation and multipath search algorithm to locate the tumor ROI quickly, which outperformed the tumor location approaches utilizing fixed and inflexible constraints. Shao et al. [154] detected tumor in BUS image by estimating tumor's saliency; the approach modeled both the radiologists' attention mechanism and the layer structure of BUS image.

[62] and some early works [58-61] detected tumor automatically based on low-level image features, e.g., intensity and gradient, which made these approaches quite fast; but they strongly depended on image enhancement. The approaches [54, 55, 113, 106] constructing empirical formulas to model domain priors provided effective means for tumor detection, but the fixed RP formulated in these approaches limited their robustness and flexibility. *One direction to improve these approaches is to model more robust prior, e.g., adaptive RP [22]; the second direction is to improve the generality of the formulas by constructing them in a learning-based framework.* Learning based fully automatic approaches [25, 64, 98, 100] are promising and drawing increasing popularity recently. *There are two directions to improve these approaches: (1) incorporating both global and local features into the learning framework; and (2) learning deep representation of breast structure towards the better understanding of BUS image by using deep convolutional neural network.*

[22, 115, 154] obtain fully automatic BUS image segmentation modeling biological priors of BUS images or visual attention mechanism, which open new avenues for fully automatic BUS

image segmentation; *one possible improvement is to utilize the learning-based framework to learn the empirical parameter adaptively and automatically.*

7.3 Modeling Prior Knowledge

Many ordinary image segmentation frameworks have been applied to BUS image segmentation; however, just applying ordinary image segmentation approaches only can achieve poor performance; and successful BUS segmentation approaches should model domain-related priors appropriately. We summarize the major priors that have been modeled in BUS image segmentation as follows.

Intensity distribution. It is widely used in BUS image segmentation, and the approaches can be classified into following categories: (1) using empirical distribution to model the intensity distribution of tumor or normal tissues, e.g., Gaussian, Raleigh, exponential model, etc; (2) defining intensity distribution implicitly by using histograms and classifiers. In graph-based approaches [7, 9 - 11], Gaussian distribution of tumor intensity is usually applied to define the likelihood energy (data term). Liu et al. [67] model the probability density difference between the intensity distribution of tumor/background region and estimated Rayleigh distribution to improve the performance of GDM. In [22, 54, 55], no explicit distribution was predefined, and histogram was applied to describe the distribution of tumor region and normal tissues; In [25, 27, 28], supervised learning approaches are introduced to train the classifiers to output the probability of each image region to be tumor or background.

Texture and local region statistics. Texture and other local region features have more descriptive power than intensity, and have been studied in many works [9, 10, 64, 98] that they can distinguish tumor regions from normal tissues with high accuracy. In [9, 10], the texture distributions are utilized to build the likelihood energy of the graph model. Madabhushi et al. [54, 55] trained a texture histogram of tumor regions, and incorporated it with the trained intensity distribution to determine the candidate tumor regions. Liu et al. [64, 98] extracted statistic texture from local regions (16×16 grid), and learned a SVM classifier that could localize tumors accurately.

Edge or gradient. In edge-based DMs, [42, 50, 52, 56 - 59, 61 - 63], image gradient is applied to constructing the external force or speed function of the evolving curve; as discussed in section 3.3, because of the speckle noise and weak boundary problems, the performance of most approaches depends on both denoising and edge preservation techniques; [73, 75] defined the stop function of GDM for edge detection results in the frequency domain rather than in the spatial domain, which makes the GDM insensitive to image contrast and work well on weak boundaries. Xian et al. [22, 115] proposed an edge detector in the frequency domain and incorporate it into a graph-based framework, which made the pairwise energy less sensitive to image contrast and brightness.

Layer structure. The breast is composed of different layers of tissues, e.g., skin, premammary, mammary, retromammary, muscle layers. Due to the difference of their physical properties, different layers have different appearances in BUS images. The location and depth of these layers may

have great variation, that makes them difficult to detect; however, some works [22, 115, 154] have utilized the layer structure information to segment breast tumors.

Topological properties. Human vision system is very sensitive to the topological properties of objects, and some works have been investigated [115, 152, 153] for both natural and medical image processing tasks. In [152, 153], the Neutro-Connectedness (NC) is proposed to compute both the connectedness structure and map, which has solve the problems of high interaction intensity and interaction-dependence in interactive image segmentation successfully; and [115] utilized the NC to solve the weak boundary of BUS images.

Smoothness. In graph-based models, it corresponds the smoothness term (pairwise energy), and the minimization of the energy makes the models produce a smooth boundary; however, it is important to notice that the smoothness term also makes the models have the tendency to shrink, and high weight of this term will cause the “shrink problem” that generates much shorter boundary than the real boundary.

Table 6. Quantitative metrics for BUS image segmentation

Metrics	Definition	Alias in References
True positive ratio (TPR)	$ R \cap G / G $	Recall rate, overlap fraction,
False negative ratio (FNR)	$1 - \text{TPR}$	None
False positive ratio (FPR)	$ R \cup G - G / G $	Error fraction
Jaccard index (JI)	$ R \cap G / R \cup G $	Similarity Index, coincidence percentage
Dice's coefficient (DSC)	$2 R \cap G /(R + G)$	Similarity Index, Dice similarity
Area error ratio (AER)	$ (R \cup G) - (R \cap G) / G $	Difference ratio, normalize residual value
Hausdorff distance (HD)	$\max \left\{ \max_{x \in R} \{d(x, G)\}, \max_{y \in G} \{d(y, R)\} \right\}$ $d(x, C) = \min_{y \in C} \{\ x - y\ \}, C = R \text{ or } G$	None
Mean absolute distance (MAD)	$1/2 \left(\sum_{x \in R} \frac{d(x, G)}{N_R} + \sum_{y \in G} \frac{d(y, R)}{N_G} \right)$	Mean error distance

7.4 Validation: ground truth, metrics, and BUS image datasets

Most BUS image segmentation approaches discussed in this paper have been evaluated quantitatively, and two major approaches have been utilized. The first approach is to evaluate segmentation performance by using physical phantoms or simulation software, e.g., Field II [155, 156]. The advantage of this approach is that the ground truth is very accurate; but the physical phantoms cannot represent the real breast anatomy exactly, and the simulation software uses simple acquisition model and cannot represent the real BUS image acquisition process well. The second approach for validation is to compare the segmentation result with manually delineated boundary. The problem of this approach is that the manually delineated ground truth could be flawed because of human error; however, this problem could be solved by labeling the boundary multiple times by same person and/or multiple radiologists. Currently, evaluating BUS image segmentation approaches through the ground truth delineated by radiologists is widely acceptable.

In BUS Image segmentation, many quantitative metrics utilized. In Table 5, we list eight commonly used metrics; the first six are area metrics and the last two are boundary metrics. Notice that in some papers [127, 137, 23, 22, 115], the similarity index (SI) refers to Jaccard index (JI), but in paper [61], SI is defined as the Dice's coefficient (DSC); for clarity, we recommend to use the original names of the two metrics, JI and DSC, instead. FNR equals to $1 - \text{TRP}$; therefore, it is not necessary to present both.

Currently, there is no public BUS image benchmark with a reasonable number of clinical cases; and the performance of most approaches are validated by only using private datasets; it is difficult

to compare different approaches objectively; therefore, there is a pressing need for establishing a BUS image benchmark. It will be valuable for comparing existing methods/algorithms by using a public dataset objectively, and for determining which approach achieves better performance and what segmentation strategies should pursue. We are building a BUS image benchmark for such purpose which can be accessed from the website <http://cvprp.cs.usu.edu/busbench>.

8. Conclusions and Future Directions

In this paper, we reviewed the automatic BUS image segmentation approaches. First, we classified all the approaches into four major categories based on the fundamental technical principles. Second, in sections 2 – 5, we presented the theoretical principles of each method, discussed their advantages and disadvantages, and summarized the strategies for BUS image segmentation. Third, in section 6, approaches of other three small sub-categories are briefly discussed. Fourth, in section 7, we discussed four fundamental open issues in BUS image segmentation and summarized the future research directions.

Unconstrained BUS image segmentation techniques: currently, most BUS image segmentation approaches work well on BUS images collected in controlled settings such as high image contrast, less artifacts, containing only one tumor per image, etc. However, their performance degrades greatly with BUS images having large variations in image quality, degree and location of artifacts, and number of tumors per image. Therefore, to promote the application of BUS CAD systems in clinical practice, it is crucial to develop unconstrained BUS segmentation techniques

which are invariant to image settings. One potential direction is to learn invariant and discriminative representations of tumors in BUS images.

Benchmark: A publicly accessible BUS image benchmark can be valuable to compare existing approaches, to discover useful strategies that can contribute to better segmentation performance, to help researchers to develop better approaches, and to eventually promote the development and advance of breast cancer research. Building of a publicly accessible BUS image dataset requires incredible effort (many years of hard work, and large amount of resources); however, its impact will be significant and profound. **(introduce our work)**

Deep learning: in the last several years, deep learning has demonstrated impressive performance for many tasks such as object recognition [158], image classification [159], semantic segmentation [160], medical applications [161], facial expression recognition [163], speech recognition [164], etc. Deep learning models have large potential to achieve good performance for BUS image segmentation because of their ability to characterize large image variations and to learn compact image representation using sufficiently large BUS image dataset.

High performance segmentation: performance is evaluated by memory cost, speed, and accuracy. Currently, many BUS image segmentation approaches are computation and memory intensive, which limits their widespread applications. For example, it is difficult to integrate resource-intensive algorithms into portable BUS devices for real time applications. In some resource-limited regions or countries, many lives lost because of unavailability of accurate and low-cost breast cancer detection techniques and devices; high performance approaches consume much less resources

than traditional resource-intensive approaches, and is vital important to provide an affordable means for breast cancer early detection.

References

- [1] R.L. Siegel, K.D. Miller, A. Jemal, Cancer statistics, 2015, *CA-Cancer J. Clin.* 65 (2015) 5-29.
- [2] L. Fan, K. Strasser-Weippl, J.-J. Li, J. St Louis, D.M. Finkelstein, K.-D. Yu, W.-Q. Chen, Z.-M. Shao, P.E. Goss, Breast cancer in China, *Lancet Oncol.* 15 (2014) e279-e289.
- [3] K. Drukker, M.L. Giger, C.J. Vyborny, E.B. Mendelson, Computerized detection and classification of cancer on breast ultrasound, *Acad. Radiol.* 11 (2004) 526-535.
- [4] H.D. Cheng, J. Shan, W. Ju, Y.H. Guo, L. Zhang, Automated breast cancer detection and classification using ultrasound images: a survey, *Pattern Recognit.* 43 (2010) 299-317.
- [5] C.M. Bishop, *Pattern recognition and machine learning*, Springer, New York, NY, 2006.
- [6] J.M. Hammersley, P. Clifford, Markov field on finite graphs and lattices, (1971).
- [7] E.A. Ashton, K.J. Parker, Multiple resolution Bayesian segmentation of ultrasound images, *Ultrason. Imaging* 17 (1995) 291-304.
- [8] T.N. Pappas, An adaptive clustering algorithm for image segmentation, *IEEE Trans. Signal Process.* 40 (1992) 901-914.
- [9] D. Boukerroui, O. Basset, N. Guerin, A. Baskurt, Multiresolution texture based adaptive clustering algorithm for breast lesion segmentation, *EJU* 8 (1998) 135-144.
- [10] D. Boukerroui, A. Baskurt, J.A. Noble, O. Basset, Segmentation of ultrasound images-multiresolution 2D and 3D algorithm based on global and local statistics, *Pattern Recognit. Lett.* 24 (2003) 779-790.

- [11] G. Xiao, M. Brady, J.A. Noble, Y. Zhang, Segmentation of ultrasound B-mode images with intensity inhomogeneity correction, *IEEE TMI* 21 (2002) 48-57.
- [12] G. Pons, J. Martí, R. Martí, J.A. Noble, Simultaneous lesion segmentation and bias correction in breast ultrasound images, in: *Pattern Recognition and Image Analysis*, Springer, 2011, pp. 692-699.
- [13] G. Pons, J. Martí, R. Martí, S. Ganau, J.A. Noble, Breast-lesion segmentation combining B-mode and elastography ultrasound, *Ultrason. Imaging* 38 (2016) 209-224.
- [14] S. Geman, D. Geman, Stochastic relaxation, Gibbs distributions, and the Bayesian restoration of images, *IEEE TPAMI* (1984) 721-741.
- [15] J. Besag, On the statistical analysis of dirty pictures, *J. R. Stat. Soc. Series B* (1986) 259-302.
- [16] D.M. Greig, B.T. Porteous, A.H. Seheult, Exact maximum a posteriori estimation for binary images, *J. R. Stat. Soc. Series B (Methodol.)* (1989) 271-279.
- [17] S. Roy, I.J. Cox, A maximum-flow formulation of the n-camera stereo correspondence problem, in: *IEEE ICCV*, Bombay, India, 1998, pp. 492-499.
- [18] Y. Boykov, O. Veksler, R. Zabih, Fast approximate energy minimization via graph cuts, *IEEE TPAMI* 23 (2001) 1222-1239.
- [19] L.R. Ford, D.R. Fulkerson, Maximal flow through a network, *Can. J. Math.* 8 (1956) 399-404.
- [20] V. Kolmogorov, R. Zabih, What energy functions can be minimized via graph cuts?, *IEEE TPAMI* 26 (2004) 147-159.
- [21] Y. Boykov, V. Kolmogorov, An experimental comparison of min-cut/max-flow algorithms for energy minimization in vision, *IEEE TPAMI*. 26 (2004) 1124-1137.

- [22] M. Xian, Y. Zhang, H.D. Cheng, Fully automatic segmentation of breast ultrasound images based on breast characteristics in space and frequency domains, *Pattern Recognit.*, 48 (2015) 485-497.
- [23] M. Xian, J. Huang, Y. Zhang, X. Tang, Multiple-domain knowledge based MRF model for tumor segmentation in breast ultrasound images, in: *IEEE ICIP*, 2012, pp. 2021-2024.
- [24] H.-H. Chiang, J.-Z. Cheng, P.-K. Hung, C.-Y. Liu, C.-H. Chung, C.-M. Chen, Cell-based graph cut for segmentation of 2D/3D sonographic breast images, in: *IEEE ISBI*, 2010, pp. 177-180.
- [25] J. Zhang, S.K. Zhou, S. Brunke, C. Lowery, D. Comaniciu, Database-guided breast tumor detection and segmentation in 2d ultrasound images, in: *SPIE MI*, 2010, pp. 7624051-7624057.
- [26] Z. Tu, Probabilistic boosting-tree: Learning discriminative models for classification, recognition, and clustering, in: *IEEE ICCV*, 2005, pp. 1589-1596.
- [27] Z. Hao, Q. Wang, H. Ren, K. Xu, Y. K. Seong, J. Kim, Multiscale superpixel classification for tumor segmentation in breast ultrasound images, in: *IEEE ICIP*, 2012, pp. 2817-2820.
- [28] Z. Hao, Q. Wang, X. Wang, J.B. Kim, Y. Hwang, B.H. Cho, P. Guo, W.K. Lee, Learning a structured graphical model with boosted top-down features for ultrasound image segmentation, in: *MICCAI*, 2013, pp. 227-234.
- [29] P.F. Felzenszwalb, R.B. Girshick, D. McAllester, D. Ramanan, Object detection with discriminatively trained part-based models, *IEEE TPAMI* 32 (2010) 1627-1645.
- [30] I. Tsochantaridis, T. Hofmann, T. Joachims, Y. Altun, Support vector machine learning for interdependent and structured output spaces, in: *ACM ICML*, Menlo Park, CA, 2004, pp. 1-8.
- [31] J. Shi, J. Malik, Normalized cuts and image segmentation, *IEEE TPAMI* 22 (2000) 888-905.

- [32] L. Gao, W. Yang, Z. Liao, X. Liu, Q. Feng, W. Chen, Segmentation of ultrasonic breast tumors based on homogeneous patch, *Med. Phys.* 39 (2012) 3299-3318.
- [33] M. Alemán-Flores, L. Álvarez, V. Caselles, Texture-oriented anisotropic filtering and geodesic active contours in breast tumor ultrasound segmentation, *J. Math. Imaging Vis.* 28 (2007) 81-97.
- [34] X. Liu, Z. Huo, J. Zhang, Automated segmentation of breast lesions in ultrasound images, in: *IEEE EMBS*, 2005, pp. 7433-7435.
- [35] R. Szeliski, R. Zabih, D. Scharstein, O. Veksler, V. Kolmogorov, A. Agarwala, M. Tappen, C. Rother, A comparative study of energy minimization methods for markov random fields, in: *IEEE ECCV*, 2006, pp. 16-29.
- [36] V. Koltun, Efficient inference in fully connected crfs with gaussian edge potentials, *Adv. Neural Inf. Process. Syst.* 2 (2011) 4.
- [37] D. Terzopoulos, On matching deformable models to images, in: *Topical Meeting on Machine Vision Tech. Digest Series*, 1987, pp. 160-167.
- [38] M. Kass, A. Witkin, D. Terzopoulos, Snakes: Active contour models, *IJCV* 1 (1988) 321-331.
- [39] L.D. Cohen, On active contour models and balloons, *CVGIP: Image Underst.* 53 (1991) 211-218.
- [40] V. Caselles, F. Catté, T. Coll, F. Dibos, A geometric model for active contours in image processing, *Numer. Math.* 66 (1993) 1-31.
- [41] R. Malladi, J.A. Sethian, B.C. Vemuri, Shape modeling with front propagation: A level set approach, *IEEE TPAMI* 17 (1995) 158-175.

- [42] A. Yezzi Jr, S. Kichenassamy, A. Kumar, P. Olver, A. Tannenbaum, A geometric snake model for segmentation of medical imagery, *IEEE TMI* 16 (1997) 199-209.
- [43] S. Kichenassamy, A. Kumar, P. Olver, A. Tannenbaum, A. Yezzi Jr, Conformal curvature flows: from phase transitions to active vision, *Arch. Ration. Mech. Anal.* 134 (1996) 275-301.
- [44] V. Caselles, R. Kimmel, G. Sapiro, Geodesic active contours, *IJCV* 22 (1997) 61-79.
- [45] J.A. Sethian, *Level set methods and fast marching methods: evolving interfaces in computational geometry, fluid mechanics, computer vision, and materials science*, Cambridge university press, 1999.
- [46] S. Osher, R. Fedkiw, *Level set methods and dynamic implicit surfaces*, Springer Science & Business Media, 2006.
- [47] C. Li, C. Xu, C. Gui, M.D. Fox, Distance regularized level set evolution and its application to image segmentation, *IEEE TIP* 19 (2010) 3243-3254.
- [48] C. Li, C. Xu, C. Gui, M.D. Fox, Level set evolution without re-initialization: a new variational formulation, in: *IEEE CVPR*, 2005, pp. 430-436 vol. 431.
- [49] C. Li, C.-Y. Kao, J.C. Gore, Z. Ding, Minimization of region-scalable fitting energy for image segmentation, *IEEE TIP* 17 (2008) 1940-1949.
- [50] Y. Chen, K.C. Keong, S.-B. Wee, Q. Zou, Adaptive expanding B-snake model for extracting ultrasound breast lump boundary, in: *IEEE ANZIIS*, 2001, pp. 19-23.
- [51] S. Menet, P. Saint-Marc, G. Medioni, Active contour models: Overview, implementation and applications, in: *IEEE SMC*, 1990, pp. 194-199.

- [52] C.-M. Chen, H.H.-S. Lu, Y.-S. Huang, Cell-based dual snake model: a new approach to extracting highly winding boundaries in the ultrasound images, *Ultrasound Med. Biol.* 28 (2002) 1061-1073.
- [53] S.R. Gunn, M.S. Nixon, A robust snake implementation: a dual active contour, *IEEE TPAMI* 19 (1997) 63-68.
- [54] A. Madabhushi, D. Metaxas, Automatic boundary extraction of ultrasonic breast lesions, in: *IEEE ISBI*, 2002, pp. 601-604.
- [55] A. Madabhushi, D.N. Metaxas, Combining low-, high-level and empirical domain knowledge for automated segmentation of ultrasonic breast lesions, *IEEE TMI* 22 (2003) 155-169.
- [56] B. Sahiner, A. Ramachandran, H.-P. Chan, M.A. Roubidoux, L.M. Hadjiiski, M.A. Helvie, N. Petrick, C. Zhou, Three-dimensional active contour model for characterization of solid breast masses on three-dimensional ultrasound images, in: *SPIE MI*, 2003, pp. 405-413.
- [57] B. Sahiner, H.-P. Chan, M.A. Roubidoux, M.A. Helvie, L.M. Hadjiiski, A. Ramachandran, C. Paramagul, G.L. LeCarpentier, A. Nees, C. Blane, Computerized characterization of breast masses on three-dimensional ultrasound volumes, *Med. Phys.* 31 (2004) 744-754.
- [58] R.-F. Chang, W.-J. Wu, W.K. Moon, W.-M. Chen, W. Lee, D.-R. Chen, Segmentation of breast tumor in three-dimensional ultrasound images using three-dimensional discrete active contour model, *Ultrasound Med. Biol.* 29 (2003) 1571-1581.
- [59] D.-R. Chen, R.-F. Chang, W.-J. Wu, W.K. Moon, W.-L. Wu, 3-D breast ultrasound segmentation using active contour model, *Ultrasound Med. Biol.* 29 (2003) 1017-1026.

- [60] R.N. Czerwinski, D.L. Jones, W.D. O'Brien Jr, Detection of lines and boundaries in speckle images-application to medical ultrasound, *IEEE TMI*, 18 (1999) 126-136.
- [61] Y.-L. Huang, D.-R. Chen, Automatic contouring for breast tumors in 2-D sonography, in: *IEEE EMBS*, 2006, pp. 3225-3228.
- [62] M. Yap, E.A. Edirisinghe, H.E. Bez, Fully automatic lesion boundary detection in ultrasound breast images, in: *SPIE MI*, 2007, pp. 651231I-651231I8.
- [63] J. Deng, H.T. Tsui, A fast level set method for segmentation of low contrast noisy biomedical images, *Pattern Recogn Lett*, 23 (2002) 161-169.
- [64] B. Liu, H.D. Cheng, J.H. Huang, J.W. Tian, J.F. Liu, X.L. Tang, Automated Segmentation of Ultrasonic Breast Lesions Using Statistical Texture Classification and Active Contour Based on Probability Distance, *Ultrasound Med. Biol.*, 35 (2009) 1309-1324.
- [65] W. Gómez, A. Infantosi, L. Leija, W. Pereira, Active Contours without Edges Applied to Breast Lesions on Ultrasound, in: *Springer MEDICON*, 2010, pp. 292-295.
- [66] T.F. Chan, L.A. Vese, Active contours without edges, *IEEE TIP* 10 (2001) 266-277.
- [67] B. Liu, H. Cheng, J. Huang, J. Tian, X. Tang, J. Liu, Probability density difference-based active contour for ultrasound image segmentation, *Pattern Recogn.* 43 (2010) 2028-2042.
- [68] N. Paragios, R. Deriche, Geodesic active contours and level sets for the detection and tracking of moving objects, *IEEE TPAMI* 22 (3) (2000) 266-280.
- [69] A. Rodtook, S.S. Makhanov, Continuous force field analysis for generalized gradient vector flow field, *Pattern Recogn.* 43 (2010) 3522-3538.

- [70] C. Xu, J.L. Prince, Generalized gradient vector flow external forces for active contours, *Signal Process.* 71 (1998) 131-139.
- [71] M.I. Daoud, M.M. Baba, F. Awwad, M. Al-Najjar, E.S. Tarawneh, Accurate Segmentation of Breast Tumors in Ultrasound Images Using a Custom-Made Active Contour Model and Signal-to-Noise Ratio Variations, in: *IEEE SITIS*, 2012, pp. 137-141.
- [72] S. Lobregt, M.A. Viergever, A discrete dynamic contour model, *IEEE TMI* 14 (1995) 12-24.
- [73] L. Gao, X. Liu, W. Chen, Phase-and gvf-based level set segmentation of ultrasonic breast tumors, *J Appl. Math.* 2012 (2012) 1-22.
- [74] P. Kovessi, Phase congruency: A low-level image invariant, *Psychological Research Psychologische Forschung*, 64 (2000) 136-148.
- [75] L. Cai, Y. Wang, A phase-based active contour model for segmentation of breast ultrasound images, in: *IEEE BMEI*, 2013, pp. 91-95.
- [76] Q. Lin, S. Liu, S.S. Parajuly, Y. Deng, L. Boroczky, S. Fu, Y. Wu, Y. Pen, Ultrasound lesion segmentation using clinical knowledge-driven constrained level set, in: *IEEE EMBC*, 2013, pp. 6067-6070.
- [77] S. Lankton, A. Tannenbaum, Localizing region-based active contours, *IEEE TIP* 17 (2008) 2029-2039.
- [78] Z. Liu, L. Zhang, H. Ren, J.-Y. Kim, A robust region-based active contour model with point classification for ultrasound breast lesion segmentation, in: *SPIE MI*, 2013, pp. 86701P1-86701P8.
- [79] B.H. Cho, Y.K. Seong, J. Kim, Z. Liu, Z. Hao, E.Y. Ko, K.-G. Woo, Ultrasound breast lesion segmentation using adaptive parameters, in: *SPIE MI*, 2014, pp. 90351E1-90351E6.

- [80] J. Yuan, Active contour driven by local divergence energies for ultrasound image segmentation, *IET Image Processing*, 7 (2013).
- [81] H.-C. Kuo, M.L. Giger, I. Reiser, K. Drukker, J.M. Boone, K.K. Lindfors, K. Yang, A. Edwards, C.A. Sennett, Segmentation of breast masses on dedicated breast computed tomography and three-dimensional breast ultrasound images, *JMI* 1 (2014) 0145011-01450112.
- [82] H.-C. Kuo, M.L. Giger, I. Reiser, J.M. Boone, K.K. Lindfors, K. Yang, A. Edwards, Level set segmentation of breast masses in contrast-enhanced dedicated breast CT and evaluation of stopping criteria, *J. Digit. Imaging* 27 (2014) 237-247.
- [83] M. Kupinski, M.L. Giger, Automated seeded lesion segmentation on digital mammograms, *IEEE TMI* 17 (1998) 510-517.
- [84] Y. Yuan, M.L. Giger, H. Li, K. Suzuki, C. Sennett, A dual-stage method for lesion segmentation on digital mammograms, *Med. Phys.* 34 (2007) 4180-4193.
- [85] J.C. Dunn, A fuzzy relative of the ISODATA process and its use in detecting compact well-separated clusters, *Journal of Cybernetics* 3 (1973) 32-57.
- [86] C.B. James, *Pattern recognition with fuzzy objective function algorithms*, Kluwer Academic Publishers, Norwell, MA, USA, 1981.
- [87] Y. Xu, A modified spatial fuzzy clustering method based on texture analysis for ultrasound image segmentation, in: *IEEE ISIE*, 2009, pp. 746-751.
- [88] K.-S. Chuang, H.-L. Tzeng, S. Chen, J. Wu, T.-J. Chen, Fuzzy c-means clustering with spatial information for image segmentation, *Comput. Med. Imag. Grap.* 30 (2006) 9-15.

- [89] C. Lo, Y.-W. Shen, C.-S. Huang, R.-F. Chang, Computer-aided multiview tumor detection for automated whole breast ultrasound, *Ultrason. Imaging* 36 (2014) 3-17.
- [90] D. W. Hosmer Jr, and S. Lemeshow, *Applied logistic regression*: John Wiley & Sons, 2004.
- [91] W.K. Moon, C.-M. Lo, R.-T. Chen, Y.-W. Shen, J.M. Chang, C.-S. Huang, J.-H. Chen, W.-W. Hsu, R.-F. Chang, Tumor detection in automated breast ultrasound images using quantitative tissue clustering, *Med. Phys.* 41 (2014) 042901.
- [92] Y.Z. Cheng, Mean Shift, Mode Seeking, and Clustering, *IEEE TPAMI* 17 (1995) 790-799.
- [93] American College of Radiology, *Breast imaging reporting and data system atlas (BI-RADS atlas)*, Reston, VA: American College of Radiology, vol. 98, 2003.
- [94] J. Shan, A fully automatic segmentation method for breast ultrasound images, Dissertation, Utah State University, 2011.
- [95] J. Shan, H. Cheng, Y. Wang, A novel segmentation method for breast ultrasound images based on neutrosophic l-means clustering, *Med. Phys.* 39 (2012) 5669-5682.
- [96] B.E. Boser, I.M. Guyon, V.N. Vapnik, A training algorithm for optimal margin classifiers, in: *ACM Computational learning theory*, 1992, pp. 144-152.
- [97] C. Cortes, V. Vapnik, Support-vector networks, *Machine Learning* 20 (1995) 273-297.
- [98] B. Liu, H.D. Cheng, J.H. Huang, J.W. Tian, X.L. Tang, J.F. Liu, Fully automatic and segmentation-robust classification of breast tumors based on local texture analysis of ultrasound images, *Pattern Recognit.* 43 (2010) 280-298.
- [99] V. Vapnik, *Statistical Learning Theory*, Wiley-Interscience, New York, 1998.

- [100] P. Jiang, J. Peng, G. Zhang, E. Cheng, V. Megalooikonomou, H. Ling, Learning-based automatic breast tumor detection and segmentation in ultrasound images, in: IEEE ISBI, 2012, pp. 1587-1590.
- [101] Y. Freund, R.E. Schapire, A decision-theoretic generalization of on-line learning and an application to boosting, *J. Comput. Syst. Sci.* 55 (1997) 119-139.
- [102] P. Viola, M.J. Jones, Robust real-time face detection, *IJCV*, 57 (2004) 137-154.
- [103] S.-F. Huang, Y.-C. Chen, W.K. Moon, Neural network analysis applied to tumor segmentation on 3D breast ultrasound images, in: IEEE ISBI, 2008, pp. 1303-1306.
- [104] A.A. Othman, H.R. Tizhoosh, Segmentation of Breast Ultrasound Images Using Neural Networks, in: Springer EANN, 2011, pp. 260-269.
- [105] J. Shan, Y. Wang, H.-D. Cheng, Completely automatic segmentation for breast ultrasound using multiple-domain features, in: IEEE ICIP, 2010, pp. 1713-1716.
- [106] J. Shan, H.D. Cheng, Y.X. Wang, Completely Automated Segmentation Approach for Breast Ultrasound Images Using Multiple-Domain Features, *Ultrasound Med. Biol.* 38 (2012) 262-275.
- [107] M.-C. Yang, C.-S. Huang, J.-H. Chen, R.-F. Chang, Whole breast lesion detection using naive Bayes classifier for portable ultrasound, *Ultrasound Med. Biol.* 38 (2012) 1870-1880.
- [108] E. Bribiesca, An easy measure of compactness for 2D and 3D shapes, *Pattern Recogn.* 41 (2008) 543-554.
- [109] Y. Ikedo, D. Fukuoka, T. Hara, H. Fujita, E. Takada, T. Endo, T. Morita, Development of a fully automatic scheme for detection of masses in whole breast ultrasound images, *Med. Phys.* 34 (2007) 4378-4388.

- [110] M. Yap, E.A. Edirisinghe, H.E. Bez, Fully automatic lesion boundary detection in ultrasound breast images, in: SPIE MI, 2007, pp. 65123I2-65123I8.
- [111] M.H. Yap, A novel algorithm for initial lesion detection in ultrasound breast images, *J. Appl. Clin. Med. Phys* 9 (2008).
- [112] S. Joo, Y.S. Yang, W.K. Moon, H.C. Kim, Computer-aided diagnosis of solid breast nodules: use of an artificial neural network based on multiple sonographic features, *IEEE TMI* 23 (2004) 1292-1300.
- [113] J. Shan, H.D. Cheng, Y.X. Wang, A novel automatic seed point selection algorithm for breast ultrasound images, in: *ICPR*, 2008, pp. 3990-3993.
- [114] R.-F. Chang, W.-J. Wu, W.K. Moon, D.-R. Chen, Automatic ultrasound segmentation and morphology based diagnosis of solid breast tumors, *Breast cancer research and treatment*, 89 (2005) 179-185.78
- [115] M. Xian, H.D. Cheng, Y. Zhang, A Fully Automatic Breast Ultrasound Image Segmentation Approach Based on Neutro-Connectedness, in: *ICPR*, 2014, pp. 2495-2500.
- [116] J.I. Kwak, M.N. Jung, S.H. Kim, N.C. Kim, 3D segmentation of breast tumor in ultrasound images, in: *SPIE, MI*, 2003, pp. 193-200.
- [117] J.I. Kwak, S.H. Kim, N.C. Kim, RD-based seeded region growing for extraction of breast tumor in an ultrasound volume, in: *Computational Intelligence and Security*, Springer, 2005, pp. 799-808.
- [118] J. Massich, F. Meriaudeau, E. Pérez, R. Martí, A. Oliver, J. Martí, Lesion segmentation in breast sonography, in: *Digital Mammography*, Springer, 2010, pp. 39-45.
- [119] S. Beucher, C. Lantuéjoul, Use of watersheds in contour detection, in: *International workshop on image processing: real-time edge and motion detection/estimation*, Rennes, France, 1979.

- [120] J. Cousty, G. Bertrand, L. Najman, M. Couprie, Watershed cuts: Minimum spanning forests and the drop of water principle, *IEEE TPAMI* 31 (2009) 1362-1374.
- [121] S. Beucher, F. Meyer, *The morphological approach to segmentation: the watershed transformation*, Optical Engineering-New York-Marcel Dekker Incorporated 34 (1992) 433-433.
- [122] Y.-L. Huang, D.-R. Chen, Watershed segmentation for breast tumor in 2-D sonography, *Ultrasound Med. Biol.*,30 (2004) 625-632.
- [123] Y. Ikedo, D. Fukuoka, T. Hara, H. Fujita, E. Takada, T. Endo, T. Morita, Computer-aided detection system of breast masses on ultrasound images, in: *SPIE MI*, 2006, pp. 61445L1-61445L8.
- [124] W. Gómez, L. Leija, A. Alvarenga, A. Infantosi, W. Pereira, Computerized lesion segmentation of breast ultrasound based on marker-controlled watershed transformation, *Med. Phys.* 37 (2010) 82-95.
- [125] W. Gómez, L. Leija, W.C.A. Pereira, A.F.C. Infantosi, Segmentation of Breast Nodules on Ultrasonographic Images Based on Marker-Controlled Watershed Transform, *Computación y Sistemas*, 14 (2010) 165-174.
- [126] M. Zhang, *Novel approaches to image segmentation based on neutrosophic logic*, PhD thesis, Utah State University, 2010.
- [127] M. Zhang, L. Zhang, H.-D. Cheng, Segmentation of ultrasound breast images based on a neutrosophic method, *Opt. Eng.* 49 (2010) 117001-117012.
- [128] C.M. Lo, R.T. Chen, Y.C. Chang, Y.W. Yang, M.J. Hung, C.S. Huang, R.F. Chang, Multi-Dimensional Tumor Detection in Automated Whole Breast Ultrasound Using Topographic Watershed, *IEEE TMI* 33 (2014) 1503-1511.

- [129] D. W. Hosmer, and S. Lemeshow, Applied logistic regression: Wiley-Interscience, 2000.
- [130] N. Otsu, A threshold selection method from gray-level histograms, *Automatica*, 11 (1975) 23-27.
- [131] J.-F. Rivest, P. Soille, S. Beucher, Morphological gradients, in: SPIE/IS&T Symposium on Electronic Imaging: Science and Technology, 1992, pp. 139-150.
- [132] K. Horsch, M.L. Giger, L.A. Venta, C.J. Vyborny, Automatic segmentation of breast lesions on ultrasound, *Med. Phys* 28 (2001) 1652-1659.
- [133] K. Horsch, M.L. Giger, L.A. Venta, C.J. Vyborny, Computerized diagnosis of breast lesions on ultrasound, *Med. Phys* 29 (2002) 157-164.
- [134] J. V. Neumann, Theory of Self-Reproducing Automata: University of Illinois Press, 1966.
- [135] V. Vezhnevets, V. Konouchine, GrowCut: Interactive multi-label ND image segmentation by cellular automata, in: proc. of Graphicon, Citeseer, 2005, pp. 150-156.
- [136] Y. Liu, H. Cheng, J. Huang, Y. Zhang, X. Tang, An effective approach of lesion segmentation within the breast ultrasound image based on the cellular automata principle, *JDI* 25 (2012) 580-590.
- [137] L. Zhu, I. Kolesov, Y. Gao, R. Kikinis, A. Tannenbaum, An effective interactive medical image segmentation method using fast growcut, in: MICCAI Workshop on Interactive Medical Image Computing, 2014.
- [138] C.-M. Chen, Y.-H. Chou, C.S. Chen, J.-Z. Cheng, Y.-F. Ou, F.-C. Yeh, K.-W. Chen, Cell-competition algorithm: A new segmentation algorithm for multiple objects with irregular boundaries in ultrasound images, *Ultrasound Med. Biol.* 31 (2005) 1647-1664.

- [139] J.-Z. Cheng, C.-M. Chen, Y.-H. Chou, C.S. Chen, C.-M. Tiu, K.-W. Chen, Cell-based two-region competition algorithm with a map framework for boundary delineation of a series of 2D ultrasound images, *Ultrasound Med. Biol.* 33 (2007) 1640-1650.
- [140] H.-H. Chiang, J.-Z. Cheng, P.-K. Hung, C.-Y. Liu, C.-H. Chung, C.-M. Chen, Cell-based graph cut for segmentation of 2D/3D sonographic breast images, in: *IEEE ISBI*, 2010, pp. 177-180.
- [141] M. Kupinski, M.L. Giger, Automated seeded lesion segmentation on digital mammograms, *IEEE TMI* 17 (1998) 510-517.
- [142] K. Drukker, M.L. Giger, K. Horsch, M.A. Kupinski, C.J. Vyborny, E.B. Mendelson, Computerized lesion detection on breast ultrasound, *Med. Phys* 29 (2002) 1438-1446.
- [143] K. Drukker, M.L. Giger, K. Horsch, C.J. Vyborny, Computerized analysis of sonograms for the detection of breast lesions, in: *SPIE MI*, 2002, pp. 1320-1324.
- [144] K. Drukker, M.L. Giger, C.J. Vyborny, R.A. Schmidt, E.B. Mendelson, M. Stern, Computerized detection and classification of lesions on breast ultrasound, in: *SPIE MI*, 2003, pp. 106-110.
- [145] H.-C. Kuo, M.L. Giger, I. Reiser, K. Drukker, A. Edwards, C.A. Sennett, Automatic 3D lesion segmentation on breast ultrasound images, in: *SPIE MI*, 2013, pp. 8670251-8670256.
- [146] L.D. Cohen, I. Cohen, Finite-element methods for active contour models and balloons for 2-D and 3-D images, *IEEE TPAMI* 15 (1993) 1131-1147.
- [147] J.M. Dias, J.M. Leitao, Wall position and thickness estimation from sequences of echocardiographic images, *IEEE TMI* 15 (1996) 25-38.
- [148] Y. Yu, S.T. Acton, Speckle reducing anisotropic diffusion, *IEEE TIP* 11 (2002) 1260-1270.

- [149] K.Z. Abd-Elmoniem, A.-B. Youssef, Y.M. Kadah, Real-time speckle reduction and coherence enhancement in ultrasound imaging via nonlinear anisotropic diffusion, *IEEE TBE* 49 (2002) 997-1014.
- [150] C. Tomasi, R. Manduchi, Bilateral filtering for gray and color images, in: *IEEE ICCV*, 1998, pp. 839-846.
- [151] M. Elad, On the origin of the bilateral filter and ways to improve it, *IEEE TIP* 11 (2002) 1141-1151.
- [152] M. Xian, Y. Zhang, H.-D. Cheng, F. Xu, J. Ding, Neutro-connectedness cut, *IEEE TIP* 25 (2016) 4691-4703.
- [153] M. Xian, F. Xu, H. D. Cheng, EISeg: Effective Interactive Segmentation, in: *ICPR*, 2016 (accepted).
- [154] H. Shao, Y. Zhang, M. Xian, H.D. Cheng, F. Xu, J. Ding, A saliency model for automated tumor detection in breast ultrasound images, in: *IEEE ICIP*, 2015, pp. 1424-1428.
- [155] J.A. Jensen, Field: A program for simulating ultrasound systems, in: *Medical & Biological Engineering & Computing*, Citeseer, 1996, pp. 351-353.
- [156] J.A. Jensen, N.B. Svendsen, Calculation of pressure fields from arbitrarily shaped, apodized, and excited ultrasound transducers, *IEEE TUFFC* 39 (1992) 262-267.
- [157] Y. Zhang, H.D. Cheng, J. Tian, J. Huang, X. Tang, Fractional subpixel diffusion and fuzzy logic approach for ultrasound speckle reduction, *Pattern Recogn*, 43 (2010) 2962-2970.
- [158] D. Cireşan, U. Meier, J. Masci, J. Schmidhuber, Multi-column deep neural network for traffic sign classification, *Neural Networks*, 32 (2012) 333-338.
- [159] D. Ciregan, U. Meier, J. Schmidhuber, Multi-column deep neural networks for image classification, in: *IEEE CVPR*, 2012, pp. 3642-3649.

- [160] J. Long, E. Shelhamer, T. Darrell, Fully convolutional networks for semantic segmentation, in: IEEE CVPR, 2015, pp. 3431-3440.
- [161] J.-Z. Cheng, D. Ni, Y.-H. Chou, J. Qin, C.-M. Tiu, Y.-C. Chang, C.-S. Huang, D. Shen, C.-M. Chen, Computer-Aided diagnosis with deep learning architecture: applications to breast lesions in us images and pulmonary nodules in CT scans, *Scientific reports*, 6 (2016).
- [162] L. Deng, D. Yu, Deep learning: methods and applications, *Foundations and Trends in Signal Processing*, 7 (2014) 197-387.
- [163] P.O. Glauner, Deep convolutional neural networks for smile recognition, arXiv preprint arXiv:1508.06535, (2015).
- [164] L. Deng, G. Hinton, B. Kingsbury, New types of deep neural network learning for speech recognition and related applications: An overview, in: IEEE ICASSP, 2013, pp. 8599-8603.
- [165] Q.-H. Huang, S.-Y. Lee, L.-Z. Liu, M.-H. Lu, L.-W. Jin, A.-H. Li, A robust graph-based segmentation method for breast tumors in ultrasound images, *Ultrasonics*, 52 (2012) 266-275.
- [166] Q. Huang, X. Bai, Y. Li, L. Jin, X. Li, Optimized graph-based segmentation for ultrasound images, *Neurocomputing*, 129 (2014) 216-224.